

Multiple Andreev Reflection Effects in Asymmetric STM Josephson Junctions

Wan-Ting Liao,^{1,2} S. K. Dutta,² R. E. Butera,¹
C. J. Lobb,^{2,3} F. C. Wellstood,^{2,3} and M. Dreyer¹

¹*Laboratory for Physical Sciences, College Park, Maryland 20740*

²*Quantum Materials Center, Department of Physics,
University of Maryland, College Park, Maryland 20742*

³*Joint Quantum Institute, University of Maryland, College Park, Maryland 20742*

(Dated: January 16, 2026)

Abstract

We have examined the electrical behavior of Josephson junctions formed by a scanning tunneling microscope (STM) with a Nb sample and a Nb tip, with normal-state resistances R_n varying between $1\text{ k}\Omega$ and $10\text{ M}\Omega$. Current-voltage characteristics were obtained as a function of R_n by varying the distance between the tip and sample at temperatures of 50 mK and 1.5 K . R_n decreases as the tip-sample separation is reduced, and the junction evolves from a phase-diffusion regime to an underdamped small junction regime, and then to a point contact regime. The subgap structure exhibits pronounced multiple Andreev reflection (MAR) features whose amplitudes and onset energies depend sensitively on junction transparency and gap asymmetry. To interpret these spectra, we generalize the Averin–Bardas MAR theory to superconductors with unequal gap magnitudes, providing a quantitative model appropriate for asymmetric STM junctions. The resulting fits yield the superconducting gaps of the electrodes, barrier transparency, and number of conduction channels as a function of R_n . Combining this analysis with Josephson junction dynamics, we further account for the observed switching and retrapping currents and the finite resistance of the supercurrent branch. Our results demonstrate that incorporating intrinsic electrode asymmetry is essential for reliably extracting transport parameters in STM-based superconducting weak links.

I. INTRODUCTION

When electrical current flows freely across a good metallic contact, the voltage drop reflects the normal resistivity of the materials. In contrast, when two conductors are connected through a "weak link," the coupling between them is limited by the transmission through a small number of electronic channels. For example, when the weak link couples two superconductors, a Josephson junction is formed [1]. In the pioneering work of Scheer *et al.* [2], atomic-scale superconducting break-junctions were fabricated using an STM (scanning tunneling microscope) technique [3–6] or by controllably bending a thin film, forming symmetric Josephson junctions. The transport properties of such junctions are governed by the intrinsic properties of the electrodes and the microscopic details of the coupling region, giving rise to phenomena such as Josephson supercurrents and multiple Andreev reflection (MAR) [2, 4, 7–13]. Through MAR spectroscopy, they observed individual channels linked to the atomic chemical valence of the material, establishing MAR as a powerful probe of

superconducting transport.

A Josephson STM [14–23] provides a complementary platform for investigating atomic scale superconducting junctions. A key advantage of this platform is the ability to tune the weak-link properties *in situ* by varying the tip–sample separation, thereby controlling the normal-state resistance R_n . Recently, MAR theory combined with $P(E)$ theory has enabled a quantitative interpretation of Josephson STM measurements, relating subgap transport and Josephson currents to microscopic channel transmission [20, 22]. In Josephson STM junctions, asymmetry in superconducting energy gaps and electrode geometries is common [11, 24]. Such asymmetry can arise from the use of different STM tip and sample materials, or from preparation-induced gap variations, even for nominally identical electrodes. Similar gap mismatches are also common in other superconducting devices, such as those used for quantum computation [25].

To understand how MAR manifests in junctions with asymmetric superconducting gaps and electrode geometries, we examined how spectroscopic features in their current-voltage $I - V$ characteristics depend on the properties of the weak link. In this work, we used a cryogenic STM [26] with a Nb tip and Nb sample to form superconducting weak links. We varied the junction normal state resistances R_n between $1 \text{ k}\Omega$ to $10 \text{ M}\Omega$, enabling both voltage- and current-biased measurements of MAR subgap features and other key junction parameters such as the switching current I_s , retrapping current I_r , and supercurrent branch resistance R_z . Depending on R_n , the junction operates in the phase-diffusion regime [14, 27, 28], the underdamped small-junction limit [19, 29, 30], or the point-contact regime [3, 4].

We analyzed the resulting $I - V$ characteristics using a generalized Averin–Bardas framework [7] for the case of superconductors with different gap magnitudes, yielding an asymmetric MAR model applicable to STM junctions. By fitting to the measured $I - V$ and dI/dV characteristics, we obtained the transparency, superconducting gaps, and number of conduction channels as a function of junction resistance. We find that superconducting gap asymmetry is essential for accurately capturing the evolution of the subgap MAR structure with increasing transparency. Additional measurements allow us to explore the crossover between different transport regimes and the role of phase diffusion in small Josephson junctions.

II. THEORY

MAR has been theoretically addressed mainly by two different approaches. The first, from Averin and Bardas (AB), characterizes the current in a weak link constriction by a scattering matrix [7]. The second approach, from Cuevas *et al.*, uses a Hamiltonian of the total current through the contact, solved with nonequilibrium Green's function techniques [8]. Both assumed a symmetric junction, composed of two electrodes with the same superconducting gap. Later, Wu *et al.* [31] generalized the Hamiltonian approach for asymmetric junctions. In this section, we adapt the theoretical AB approach, which provides a vivid physical picture of the processes involved, to the case of superconductors with different gaps.

Figure 1 illustrates a generalized AB model for asymmetric MAR, which allows for different superconducting gaps in the two leads. The left lead is superconductor S_L with gap Δ_L and the right lead is superconductor S_R with gap Δ_R . A voltage bias V is applied to the right lead with respect to the left. Between the two superconductors are normal metal regions, N_L and N_R , separated by a scattering potential that sets the barrier transparency D , the probability that an incident particle is transmitted. All electron and hole scattering effects in the normal metal are incorporated into D and we assume the interface between each superconductor and the normal region has unity transparency. In the absence of scattering, the link is completely transparent and $D = 1$. Otherwise, D falls between 0 and 1. An electron in N_L that is incident on S_L , for example, may be Andreev reflected as a hole (as shown by the red dashed line), generating a Cooper pair in S_L . An analogous process occurs for an incident hole. Similarly, an electron (hole) in N_R incident on S_R may be Andreev reflected as an hole (electron).

Multiple Andreev reflections can occur because an electron traveling to the right in region N_L may pass through the barrier (with a certain probability amplitude) and then be Andreev reflected at the N_R - S_R interface, emerging as a hole in N_R . The reflected hole may then travel back through the barrier and arrive at the N_L - S_L interface where it can again be Andreev reflected with some probability amplitude. In the AB analysis, this process continues, allowing the iterative construction of the electron and hole wavefunctions in the normal regions. The wavefunctions in N_L and N_R are interdependent because the net current must be the same in both regions. The detailed nature of this dependence is determined by the barrier, and can be represented by a scattering matrix. With knowledge of the scattering

matrix, recursion relations are derived to obtain the wavefunction coefficients [7]. A detailed schematic of the Andreev process can be found in Fig. S1 in the Supplemental Material [32].

When S_L and S_R have different gaps, then the Andreev reflection amplitudes will not depend solely on the energy relative to the Fermi energy, but also on which interface is reflecting the particle. For the $N_L - S_L$ interface, the Andreev reflection amplitude of a quasiparticle with energy E is [7]

$$a^L(E) = \frac{1}{\Delta_L} \times \begin{cases} E - \text{sgn}(E)(E^2 - \Delta_L^2)^{1/2}, & |E| > \Delta_L \\ E - i(\Delta_L^2 - E^2)^{1/2}, & |E| < \Delta_L \end{cases} \quad (1)$$

and for the the right interface, it is

$$a^R(E) = \frac{1}{\Delta_R} \times \begin{cases} E - \text{sgn}(E)(E^2 - \Delta_R^2)^{1/2}, & |E| > \Delta_R \\ E - i(\Delta_R^2 - E^2)^{1/2}, & |E| < \Delta_R. \end{cases} \quad (2)$$

Because the Andreev reflection amplitudes are different at the left and right $N - S$ interfaces, it is necessary to explicitly consider hole-like quasiparticles incident from the left and right electrodes, as well as electron-like quasiparticles incident from both electrodes, for a total of four separate processes. To calculate the total current, we find the corresponding wavefunctions and sum the current from each process.

In region N_L , the wavefunctions that result from an electron-like quasiparticle incident from S_L are

$$\begin{aligned} \psi_e^{eL} &= \sum_{n=-\infty}^{\infty} [(a_{\{2n,+}\}^L A_n^{\rightarrow} + J^L \delta_{n0}) e^{+ikx} + B_n^{\rightarrow} e^{-ikx}] e^{-i(\varepsilon+2neV)t/\hbar} \\ \psi_h^{eL} &= \sum_{n=-\infty}^{\infty} [A_n^{\rightarrow} e^{+ikx} + a_{\{2n,+}\}^L B_n^{\rightarrow} e^{-ikx}] e^{-i(\varepsilon+2neV)t/\hbar}, \end{aligned} \quad (3)$$

where ψ_e^{eL} and ψ_h^{eL} represent electrons and holes, respectively. $J^L(\varepsilon) = \sqrt{1 - |a^L(\varepsilon)|^2}$ is the quasiparticle source current term from S_L . k and ε are the Fermi wavevector and energy of the incident quasiparticle, and t is the time. $a_{\{2n,+}\}^L = a^L(\varepsilon + 2neV)$ is the Andreev reflection amplitude. The wavefunction amplitudes shown in Fig. 1 only apply to the case of an electron-like quasiparticle source incident from the left, with further details given in the Supplemental Material [32].

Here, an electron acquires a total energy of $2eV$ during a cycle in which it travels from S_L to S_R through the barrier, undergoes Andreev reflection as a hole at the $N_R - S_R$ interface,

propagates back through the barrier, and is finally Andreev reflected back into an electron at the $N_L - S_L$ interface. A_n^\rightarrow and B_n^\rightarrow are the amplitudes of leftward moving holes and electrons in region N_L that result from the sum of reflecting off the barrier and transmitting through the barrier from the right interface, at order n . We use the arrow label over A_n and B_n to signify that these amplitudes came from source quasiparticles incident from the left.

Analogously to Eq. (3), in region N_L the wavefunctions produced by a hole-like quasiparticle incident from S_L are

$$\begin{aligned}\psi_h^{hL} &= \sum_{n=-\infty}^{\infty} [(a_{\{2n,-\}}^L A_n^\rightarrow + J^L \delta_{n0}) e^{-ikx} + B_n^\rightarrow e^{+ikx}] e^{-i(\varepsilon - 2neV)t/\hbar} \\ \psi_e^{hL} &= \sum_{n=-\infty}^{\infty} [A_n^\rightarrow e^{-ikx} + a_{\{2n,-\}}^L B_n^\rightarrow e^{+ikx}] e^{-i(\varepsilon - 2neV)t/\hbar}.\end{aligned}\quad (4)$$

ψ_h^{hL} and ψ_e^{hL} represent the wavefunctions of the holes and electrons, respectively, for a hole-like quasiparticle incident from the left. $a_{\{2n,-\}}^L = a^L(\varepsilon - 2neV)$ denotes the Andreev reflection amplitude. The minus sign in the energy argument arises because a hole incident from the left loses kinetic energy eV when moving from S_L to S_R . In this case, A_n^\rightarrow and B_n^\rightarrow are the amplitudes of leftward moving electrons and holes in region N_L .

The total probability current density is then

$$\begin{aligned}j_L &= \frac{\hbar}{2mi} [(\psi_e^{eL*} \nabla \psi_e^{eL} - \psi_e^{eL} \nabla \psi_e^{eL*}) + (\psi_h^{eL*} \nabla \psi_h^{eL} - \psi_h^{eL} \nabla \psi_h^{eL*})] \\ &\quad + \frac{\hbar}{2mi} [(\psi_e^{hL*} \nabla \psi_e^{hL} - \psi_e^{hL} \nabla \psi_e^{hL*}) + (\psi_h^{hL*} \nabla \psi_h^{hL} - \psi_h^{hL} \nabla \psi_h^{hL*})],\end{aligned}\quad (5)$$

where m is the mass of the quasiparticle.

The total electrical current I_L due to an electron and hole incident from the left is directly proportional to this current density. Summing over the source energy gives

$$I_L(t) = \frac{e}{2\pi\hbar} \frac{m}{\hbar k} \int_{-\infty}^{\infty} d\varepsilon j_L(\varepsilon, t) f(\varepsilon), \quad (6)$$

where $f(\varepsilon) = (e^{\varepsilon/k_B T} + 1)^{-1}$ is the electron occupancy for states at energy ε , which we assume is a Fermi distribution.

This completes half of the story. To calculate the total current $I(t)$, we also need to consider the current $I_R(t)$ due to an electron-like or hole-like quasiparticle incident from

the right. The main physics remains the same, except we need to take into account that (1) an electron-like quasiparticle loses kinetic energy eV when traveling from the right to the left interface and (2) a hole-like quasiparticle gains energy eV when traveling from the right to the left interface. Therefore, the wavefunctions ψ_e^{eR} and ψ_h^{eR} for an electron incident from the right can be found from ψ_h^{hL} and ψ_e^{hL} by substituting superscript R for L , and \leftarrow for \rightarrow . Similarly the wavefunctions ψ_h^{hR} and ψ_e^{hR} can be found from ψ_e^{eL} and ψ_h^{eL} with the same substitutions. Full expressions for these wavefunctions are given in the Supplemental Material [32].

Combining the left and right currents, the total junction current is

$$I_L(t) + I_R(t) = \sum_k I_k e^{i2keVt/\hbar}, \quad (7)$$

where

$$\begin{aligned} I_k = & \frac{e}{2\pi\hbar} \left[2eVD\delta_{k0} - \int_{-\infty}^{\infty} d\varepsilon \tanh\left(\frac{\varepsilon}{2k_B T}\right) \left(J^L(\varepsilon)[(a_{2k}^{\rightarrow})^*(A_k^{\rightarrow})^* + a_{-2k}^{\rightarrow} A_{-k}^{\rightarrow}] \right. \right. \\ & + \sum_n [1 + a_{2n}^{\rightarrow} (a_{2(n+k)}^{\rightarrow})^*] [A_n^{\rightarrow} (A_{n+k}^{\rightarrow})^* - B_n^{\rightarrow} (B_{n+k}^{\rightarrow})^*] \left. \right) + \int_{-\infty}^{\infty} d\varepsilon \tanh\left(\frac{\varepsilon}{2k_B T}\right) \\ & \left. \left(J^R(\varepsilon)[a_{2k}^{\leftarrow} A_k^{\leftarrow} + (a_{-2k}^{\leftarrow})^* (A_{-k}^{\leftarrow})^*] + \sum_n [1 + (a_{2n}^{\leftarrow})^* a_{2(n+k)}^{\leftarrow}] [(A_n^{\leftarrow})^* A_{n+k}^{\leftarrow} - (B_n^{\leftarrow})^* B_{n+k}^{\leftarrow}] \right) \right] \right]. \end{aligned} \quad (8)$$

Here we have simplified the sums by defining $a_n^{\rightarrow} = a^R(\varepsilon + neV)$ for n odd and $a_n^{\rightarrow} = a^L(\varepsilon + neV)$ for n even. Thus, an odd valued subscript corresponds to a component that had an Andreev reflection from S_R and an even subscript to Andreev reflection from S_L . Similarly $a_n^{\leftarrow} = a^L(\varepsilon - neV)$ for n odd and $a_n^{\leftarrow} = a^R(\varepsilon - neV)$ for n even; the odd indices are for S_L and the even indices are for S_R .

To calculate the $I - V$ characteristic, we need to know the amplitudes A_n^{\rightarrow} , B_n^{\rightarrow} , A_n^{\leftarrow} , and B_n^{\leftarrow} . Following AB's approach [7], we let C_n^{\rightarrow} and D_n^{\rightarrow} denote the wavefunction amplitudes in N_R (shown in Fig. 1). Relating the incoming electrons to the outgoing electrons in regions N_L and N_R using a scattering matrix S_e where

$$S_e = \begin{pmatrix} r & t \\ t & -r^*t/t^* \end{pmatrix}, \quad (9)$$

we obtain a matrix equation for electrons. Here, r and t are the normal-state reflection and transmission amplitudes of the junction at energy ε . The transparency is $D = |t|^2$. Similarly, there will be a matrix equation with a scattering matrix $S_h = S_e^*$ connecting the holes in the two regions.

After solving two matrix equations for electrons and holes (detailed derivation can be found in Ref. [33]), the wavefunction amplitudes A_n^\rightarrow and B_n^\rightarrow are

$$A_{n+1}^\rightarrow - a_{2n+1}^R a_{2n}^L A_n^\rightarrow = \sqrt{R}(a_{2n+2}^L B_{n+1}^\rightarrow - a_{2n+1}^R B_n^\rightarrow) + J^L a_1^R \delta_{n0} \quad (10)$$

$$\begin{aligned} D \frac{a_{2n+1}^R a_{2n+2}^L}{1 - (a_{2n+1}^L)^2} B_{n+1}^\rightarrow - \left[D \left(\frac{(a_{2n+1}^R)^2}{1 - (a_{2n+1}^R)^2} + \frac{(a_{2n}^L)^2}{1 - (a_{2n-1}^R)^2} \right) + 1 - (a_{2n}^L)^2 \right] B_n^\rightarrow \\ + D \frac{a_{2n}^L a_{2n-1}^R}{1 - a_{2n-1}^R} B_{n-1}^\rightarrow = -\sqrt{R} J^L \delta_{n0}, \end{aligned} \quad (11)$$

where $R = 1 - D$ is the reflection coefficient of the barrier in the normal region. The same recursion relations describe hole-like source quasiparticles incident from the left superconductor.

Similarly, to obtain the wavefunction amplitudes A_n^\leftarrow and B_n^\leftarrow for electron-like and hole-like source quasiparticles incident from the right superconductor, we swap L for R and \leftarrow for \rightarrow in Eqs. (10) and (11), by symmetry. We then plug these into Eq. (8) and obtain the Fourier components I_k using numerical integration. I_0 represents the dc current, while the junction critical current is given by [7]

$$I_c = \lim_{V \rightarrow 0} 2 |\text{Im}(I_1)|. \quad (12)$$

These currents will depend on the transparency of the junction and the superconducting gap of its two electrodes.

Figure 2 shows dc $I - V$ characteristics calculated from Eq. (8) for $D = 0.4$ with different superconducting gap ratios Δ_L/Δ_R . In the plot, the current is normalized by a factor that includes the normal-state resistance $R_n = 1/(G_0 D)$, where $G_0 = e^2/(\pi \hbar) = 1/(12.9 \text{ k}\Omega)$ is the conductance quantum. Our calculations appear to agree with previous results for $\Delta_L/\Delta_R = 1$ [7] and 0.5 [31]. The $I - V$ curves show a large subgap current compared to the low transparency tunneling limit, with steps at energies eV near Δ_L/n , Δ_R/n , and $(\Delta_L + \Delta_R)/n$ for integral values of n .

Figure 3 shows the normalized critical current calculated from Eq. (12) as a function of the transparency D for four values of the gap ratio Δ_L/Δ_R . As expected, the critical current becomes larger for larger $\Delta_L + \Delta_R$ and increases with D . For symmetric superconducting gaps, the critical current approaches the Ambegaokar-Baratoff formula $I_c R_n = \pi \Delta / 2e$ as $D \rightarrow 0$ [34]. Figure 4 shows examples of dc $I - V$ characteristics at different temperatures, for $D = 0.25$ and $\Delta_L/\Delta_R = 0.5$. At high temperature, the subgap current increases and shows thermally-rounded MAR steps.

III. EXPERIMENTAL METHODS

To perform the junction measurements, we used a custom STM mounted on the mixing chamber stage of a dilution refrigerator [26, 35]. STM tips were made from 250 μm diameter Nb wire sharpened in an SF₆ reactive ion etcher [36]. Each tip was mounted on the STM and cleaned by high-voltage field emission on an Au(100) or Au(111) single crystal under vacuum at low temperature. The superconducting sample was a 4.5 mm x 4.5 mm x 1 mm Nb(100) single crystal [37]. The sample surface was first cleaned by Ar ion sputtering with a kinetic energy of 2 keV at a pressure of 2.0×10^{-5} mbar for 3-4 h followed by annealing at 900 °C in UHV for 20 min. This cycle was repeated two or three times before the sample was transferred to the STM without breaking vacuum [26]. Figure 5 shows topographic images of the Nb surface at 1.5 K and 50 mK. Atomically flat terraces are clearly visible.

For standard STM imaging, a voltage bias V_b is applied to the sample and the tunneling current I is measured. A feedback mechanism adjusts the z -position of the tip to maintain a constant tunneling current as it is scanned in x and y , allowing one to image surface topography. $I(V)$ spectroscopy is obtained by setting a desired junction resistance, turning off the z feedback, and sweeping V_b while recording I . Subtle features of the $I(V)$ curve can be resolved by measuring dI/dV directly with a lock-in amplifier at the same time. However this mode of operation does not fully characterize low loss tunnel junctions, which may be hysteretic.

To perform current-biased measurements, a resistor $R_b \gg R_n$ is inserted in series with the junction to effectively convert the bias voltage V_b into a bias current $I_b \approx V_b/R_b$. The voltage across the junction is recorded while the bias current is swept. Figure 6 shows the schematic diagram of the voltage- and current-biased circuits we used, with a relay that

switches between the two while the tip feedback is turned off. To clearly distinguish between these two types of measurements, we specifically use $I(V)$ for voltage-biased curves (orange path in Fig. 6), and $V(I)$ for current-biased curves (green path).

IV. CURRENT-VOLTAGE CHARACTERISTICS

We next describe measurements of the $I - V$ characteristics for a range of the coupling between the tip and sample. To set each junction, feedback was established at a target setpoint current with a fixed voltage bias $V_b = 3.5$ mV. The feedback was then turned off and we measured voltage-biased $I(V)$ and dI/dV . We then switched to the current-biased mode to measure $V(I)$ for the same junction. Both measurements were taken with forward (*i.e.* increasing the current from negative to positive) and reverse sweeps. The curves were corrected to account for a contact resistance R_c (typically under $100\ \Omega$) between the sample stud and the measurement wires. We refer to each set of curves by the normal-state resistance R_n extracted from the characteristics at high voltage, where they are nearly ohmic.

Figure 7 shows $V(I)$ characteristics for three values of R_n , acquired at 1.5 K, with corresponding $I(V)$ and dI/dV curves shown in the Supplemental Material [32]. Figure 7(a) was acquired at $R_n = 57\ k\Omega$ and shows conventional low-transparency S-I-S behavior. As the current is reduced from its maximum value in the reverse sweep, the characteristic is roughly linear, with a slope of $1/R_n$. At ~ 2.1 mV, corresponding to the sum of the superconducting gaps, the current drops to near zero. We identify the quasiparticle current $I_{qp} = 33\ nA$ as the current at the intersection of the ohmic section of the voltage branch and the sudden rise at the gap edge. The current in the subgap region is small, with steps around 0.67 mV and 1.50 mV as seen more clearly in Fig. 7(b), indicating multiple Andreev reflection behavior. When the current increases from zero in the forward sweep, the junction starts in the supercurrent state with a small resistance and abruptly jumps to the voltage branch at a switching current $I_s = 620\ pA$.

In order to model the measured $I - V$ curves with the asymmetric MAR theory, we assume a total current $I(V) = \sum_{i=1}^N I_0(D_i, \Delta_s, \Delta_t, T, V)$ carried by N independent conduction channels. Here, I_0 is the dc current calculated from Eq. (8), each channel has a distinct transparency D_i , and the energy gaps of the STM sample and tip are Δ_s and Δ_t . In this

case, the total conductance is given by the Landauer formula as $G = 1/R_n = G_0 \sum_{i=1}^N D_i$. Whereas previous analyses decomposed the total conductance into channels with individually fitted transparencies [2, 10, 13, 38, 39], we find that our measurements can be described by assuming a single transparency shared across all channels, with an example shown in the Supplemental Material [32]. Thus a single transparency value can be used to characterize the transport at each R_n . The current can then be simplified as

$$I(V) = NI_0(D, \Delta_s, \Delta_t, T, V), \quad (13)$$

where N specifies a non-integral number of effective channels. The corresponding normal state resistance is $R_n = 1/(G_0 DN)$.

We chose values of Δ_s , Δ_t , D , and N to reproduce the location of peaks in dI/dV , the level of the subgap current in $V(I)$, and the resistance of the voltage branch, with T fixed at the nominal refrigerator temperature. The parameter values are listed in Table I, with the MAR characteristic calculated from Eq. (13) shown in Fig. 7. For the $R_n = 57$ k Ω data, we found that the step-like subgap features and quasiparticle current rise were reproduced for $D = 0.1$ (and thus $N = 2.26$) and superconducting gaps of 1.497 and 0.67 meV. The smaller gap is likely that of the tip, because the etching process can alter its superconducting properties. A tip gap of 0.67 meV suggests a superconducting transition temperature $T_c \approx 4.4$ K, consistent with 5% oxygen in Nb [40], which is below the solubility limit of 9%.

With the four MAR fitting parameters, Eq. (12) predicts a critical current $I_c = 26$ nA, as indicated in Fig. 7(a). The observed switching current $I_s = 620$ pA is two orders of magnitude smaller. Such large suppression has also been reported in atomic scale Nb-Nb mechanically controllable break junctions [39] and recent current-biased STM measurements [19, 29]. Note here the switching and retrapping currents are not true supercurrents because this branch of the $V(I)$ curve has a non-zero resistance of $R_z \approx 54.8$ k Ω , which will be discussed at the end of the next section.

Figure 7(c) was taken at a junction resistance of 7.9 k Ω . The lower R_n was set by using a larger feedback current, corresponding to a smaller tip-sample separation. As seen in Table I, while Δ_s only drops slightly compared to $R_n = 57$ k Ω , Δ_t decreases significantly. D increases from 0.1 to 0.27, resulting in $N = 6.05$. The subgap currents are much larger

than Fig. 7(a), as expected from D being larger, representing a more transparent tunnel barrier. The switching current in Fig. 7(d) is $I_s \approx 32$ nA, while the calculated $I_c \approx 224$ nA. Notice that the switching current in Fig. 7(c) is about 50 times larger than the switching current in Fig. 7(a), even though R_n differs by only a factor of 7. Figure 7(d) also shows hysteretic behavior with the voltage abruptly dropping to zero during the reverse sweep at a retrapping current I_r of 4.6 nA.

Figure 7(e) shows data for $R_n = 1.08$ k Ω , where the tip-sample distance was reduced further. The characteristic shows an even larger subgap current, where I_{qp} has increased to nearly 2.6 μ A, while the switching current has increased to 660 nA. In this regime, unlike the highly hysteretic behavior in Fig. 7(c), $I_r = 595$ nA is about 90% of the switching current I_s , showing a higher ratio of retrapping current with respect to the switching current for larger damping [41]. This phenomena is likely due to the tip and the sample being in point contact (Supplemental Material [32]). The fit curve in Fig. 7(e) disagrees noticeably with the data below 1.5 mV, and is very sensitive to and the transparency parameter D . As one can see, the simplified multichannel fit does not exactly reproduce the Andreev steps inside the gap. In this case, it would be natural to expect multiple channels with different transparencies D_i for low junction resistance [2, 10, 13, 38, 39].

We took similar measurements for R_n between 1 k Ω and 10 M Ω . We begin the discussion of the extracted junction properties with the characteristic currents shown in Fig. 8. Here, I_{qp} , I_s , and I_r were found directly from the $V(I)$ curves and I_c was calculated from the asymmetric MAR theory using the parameters Δ_s , Δ_t , D , N for each curve. We acquired data at 50 mK and 1.5 K to check for thermal effects and found generally good agreement between the two temperatures.

For $R_n > 100$ k Ω , no switching or retrapping currents were observed, consistent with thermal fluctuations destroying phase coherence [14, 27, 28]. For 10 k $\Omega < R_n < 100$ k Ω , a small supercurrent branch and hysteretic behavior were observed. In this regime, the switching current I_s ranges from 1% to 10% of the predicted critical current I_c (red circles), and increases rapidly as the junction resistance R_n decreases, scaling approximately as R_n^{-2} . The retrapping current I_r (triangles) increases much more rapidly than the switching current I_s as R_n decreases. Similar behavior has been observed in Refs. [19, 30]. For $R_n < 3$ k Ω , where we will argue that the tip and the sample have made solid contact, $I_r \approx I_s$. In this same range of R_n , there is a clear disagreement between the MAR theory and experimental

curve in the subgap regime below 1.5 mV.

To precisely identify the superconducting gaps of the tip and sample, we analyzed the peaks in the dI/dV data. While MAR results in a series of steps in the $I - V$ curves, and thus peaks in dI/dV , the largest occur near voltages corresponding to energies Δ_t , Δ_s , and $\Delta_s + \Delta_t$. We refer to these peak locations as the voltages V_t , V_s , and V_{st} . In Fig. 9, the extracted values for these three voltages are shown as a function of D , where the transparency values were obtained by fitting the MAR theory to the corresponding $V(I)$ curves. The peak voltages decrease with increasing D (i.e. decreasing R_n), particularly for V_{st} .

The figure also shows theoretical values of dI/dV calculated from Eq. (13) with fixed gap values of $\Delta_t = 0.657$ meV and $\Delta_s = 1.514$ meV (as indicated by the dashed lines). The peaks in dI/dV (solid lines) occur at the gap energies in the $D = 0$ tunnel limit, but shift to lower voltages with increasing transparency due to the presence of increasingly large subgap currents. A similar effect was reported in Ref. [11]. The predicted shift, however, is smaller than what is seen in the data, suggesting that the gaps themselves were changing with D in our STM measurements.

Figure 10(a) shows the same peak values, though now plotted as a function of R_n . Also shown are the values of Δ_t and Δ_s needed for the MAR theory to best reproduce the measured voltages V_t , V_s , and V_{st} (with D fixed at the fit values), where the agreement is to within 10 μ V. Δ_s is roughly constant, with a value near that of bulk Nb, while Δ_t decreases by almost 15% as R_n decreases. It shows that while some of the reduction in V_t might be coming from the bending of the MAR theory prediction, the actual gap of the tip is changing.

There are several reasons why the tip gap could decrease below $R_n = 5$ k Ω , where the junction transparency is large. One possible explanation is that the tip starts to make contact with the sample, and the tip compresses more than the sample due to its geometry. This applies pressure to the material at the end of the tip, reducing its T_c . It might also be due to the fact that pure Nb from the sample is less sensitive to pressure than oxygen-doped Nb from the tip. A third possible explanation is that a high current density in the tip causes heating, since the power dissipation is roughly 100 times higher at low D than high D . The small tip not only has a smaller thermal conductance than the sample, but if it also has a smaller T_c due to contaminants, this will lead to an even larger reduction in the

superconducting gap from heating.

Figure 10(b) shows the extracted transparency D and effective number of conduction channels N as a function of R_n from the data set in Fig. 8. As expected, $D \ll 1$ when the junction resistance R_n is high, indicating very low transparency and a junction in the standard S-I-S tunneling limit [42]. As the tip and sample get closer, R_n decreases and the transparency D becomes larger. Interestingly, D does not reach 1 for low R_n but saturates at around 0.6. The effective number of channels never decreases below 2. Similar phenomena were seen in a previous study of niobium [2]. On the other hand, when the junction resistance was small, we clearly see that N increases, as does the transparency D , indicating a higher overall transmission of the junction.

Also shown in Figure 10(b) is the transparency $D = 1 / (G_0 R_n N)$ as a function of R_n for fixed values of N . For $N = 1$, this shows the maximum transparency that any channel can have for a given value of R_n . We were not able to extract D and N for $R_n > 70$ k Ω because the subgap currents in $V(I)$ were too small to fit the MAR theory and obtain accurate results.

V. UNDERDAMPED JUNCTION PROPERTIES

Our observation of a relatively large retrapping current I_r over a large range of R_n indicates that the junction was subject to a certain amount of dissipation. Here we compare our results to the standard resistively and capacitively shunted Josephson junction (RCSJ) model [42] to extract additional junction parameters.

In the RCSJ model, the superconducting phase difference across an unbiased junction will oscillate at the plasma frequency

$$\omega_p = \sqrt{2\pi I_c / \Phi_0 C} \quad (14)$$

with a quality factor $Q = \omega_p R_e C = \sqrt{\beta_c}$. Here, $\beta_c = 2\pi I_c R_e^2 C / \Phi_0$ is the Stewart-McCumber hysteresis parameter, R_e is the total effective resistance shunting the Josephson junction, C is the total effective capacitance across the junction, and $\Phi_0 = h/2e$ is the magnetic flux quantum. If the damping is small, with $\beta_c > 1$, the junction is said to be underdamped.

In terms of the retrapping current I_r , the damping parameter is [42, 43]

$$\beta_c = (I_{qp} / I_r)^2. \quad (15)$$

Figure 11(a) shows values of β_c (black triangles) as a function of R_n at 1.5 K, extracted using this expression. Since $\beta_c \gg 1$ for all R_n , our junctions are in the relatively low dissipation limit. Using these values of β_c and assuming $I_c = \pi I_{qp}/4$, the junction capacitance is

$$C = 4\beta_c \hbar / 2eI_{qp}R_e^2\pi, \quad (16)$$

where I_{qp} is identified directly from the data (black circles in Fig. 8), and the effective resistance at the retrapping voltage V_r is

$$R_e = V_r/I_r. \quad (17)$$

Figure 11(a) also shows the resulting capacitance C as a function of R_n (red circles). The capacitance is in reasonable agreement with what one would expect for an STM tip that is near a conducting surface [18, 44–46]; the values are on the order of fF and increase as the separation between the tip and sample becomes smaller. For $R_n \geq 45$ k Ω , we could not use this approach to determine C because the retrapping current became too small to measure.

Notice that all our curves in Fig. 8 show early switching out of the supercurrent state. While the RCSJ model with MAR explains much of the observed behavior along the voltage branch, small Josephson junction physics is needed to explain the supercurrent branch. The dynamics of Josephson junctions are governed by the level of dissipation and the relative size of four different energies: the Coulomb charging energy $E_c = e^2/2C$, the Josephson energy $E_J = I_c\Phi_0/2\pi$, the thermal energy $k_B T$, and the plasma energy $\hbar\omega_p$.

Figure 11(b) shows these energies as a function of the tunneling resistance R_n . For $R_n < 10$ k Ω , $E_J > \hbar\omega_p > E_c$. In this limit, even though the quantum mechanical phase difference across the junction is relatively well defined, macroscopic quantum tunneling (MQT) [42, 47–49] can produce early switching of the supercurrent. Although there was a strong dependence of the junction behavior on R_n , we see little difference between the data taken at 50 mK (open symbols) and 1.5 K (filled symbols) in Fig. 8. The thermal energy of the junction at 50 mK was nominally 30 times smaller than at 1.5 K, but I_s was not significantly larger at 50 mK, nor was I_r significantly smaller at 50 mK.

This suggests that the switching current in our STM junction was not limited by equilibrium thermal fluctuations. One possibility is MQT of the phase, due to the small critical current and capacitance of the junction. Another possibility is external noise driving the system to switch into the voltage state. A third possibility is that the junction is at an

effective temperature that is well above the refrigerator temperature due to heating in the leads from the applied bias current. Although we can not rule out the last two alternatives, our measurements show relatively low noise.

If the junction was well-isolated from dissipation (including radiation loss), then MQT would yield an effective switching temperature of $T_{\text{esc}} = \hbar\omega_p/7.2k_B$ [48, 49]. As Fig. 11(b) shows, $T_{\text{esc}} \approx 1$ K for a wide range of R_n , which suggests MQT may be important and producing the switching currents at 50 mK that are comparable to those at 1.5 K (see Fig. 8); both are much less than the critical current obtained by fitting the MAR theory to the measured $V(I)$ curves. For R_n greater than about 10 k Ω , E_c dominates E_J . In this limit, charging effects, phase diffusion and the impedance of the bias leads become important in determining the $V(I)$ characteristic, including in particular the size of the observed phase-coherent supercurrent and the resistance of the supercurrent branch.

For small Josephson junctions, it is important to consider the effects produced by the impedance of the leads [50]. The plasma frequency ω_p of a small junction is typically 10¹⁰ Hz to 10¹¹ Hz and at such frequencies the shunting impedance Z_1 of typical bias leads has non-zero real and imaginary parts that are of order 50 Ω , which is orders of magnitude smaller than the tunneling resistance we observed. The output leads act like a mismatched transmission line, leading to high-frequency damping that increases the retrapping current and creates a non-zero resistance on the supercurrent branch due to the inelastic tunneling of Cooper pairs [30, 42, 47, 49, 51]. High frequency damping also produces noise, which causes phase diffusion, and an average voltage on the supercurrent branch. For thermally generated Nyquist noise and $E_J \ll k_B T$, one finds the supercurrent branch has a resistance [42, 52]

$$R_z = 2Z_1(k_B T/E_J)^2 = 2Z_1 \left[\frac{4e^2 k_B T R_n}{\hbar \pi \Delta} \right]^2. \quad (18)$$

Figure 12 shows a plot of R_z as a function of R_n , where R_z is the supercurrent branch resistance after subtracting off the contact resistance R_c between the sample stud and bias lines. We estimated $R_c \approx 173$ Ω at 1.5 K and $R_c \approx 0$ Ω at 50 mK. The plot shows that R_z scales quadratically with R_n , consistent with Eq. (18), suggesting that the critical current is being suppressed by phase diffusion. The extracted value of Z_1 is 820 at 1.5 K and 1776 at 50 mK.

VI. CONCLUSION

In conclusion, we used a Nb tip and Nb sample in a low temperature STM to measure the current-voltage characteristics of small superconducting Josephson junctions. By adjusting the distance between the tip and the sample, we varied the junction tunneling resistance R_n and observed $I - V$ characteristics that ranged from the low-transparency S-I-S tunneling limit to the high-transparency limit, and the superconducting gap of the tip decreased by 15% in this limit. We compared our results to simulations from a generalized Averin-Bardas model of MAR in junctions with different superconducting energy gaps. We find that the asymmetrical MAR junction theory is important for reliably extracting the superconducting gaps and the transparency of the junctions.

For R_n between 10 k Ω and 100 k Ω , the junction behaved like a hysteretic small Josephson junction with a suppressed switching current and a small but non-zero resistance R_z on the supercurrent branch. We note, in principle the full supercurrent could be observed by stabilizing the phase using a SQUID-STM configuration [24, 35, 53–55]. For $R_n < 10$ k Ω , the junction acted like a point contact. Although our MAR model does a good job of explaining many features of the $I - V$ characteristics, it leaves out potentially important physical effects, including phase diffusion, charging effects, noise, incoherent pair tunneling, and MQT. A comprehensive theory that includes all of this relevant physics, as well as MAR, is currently not available but is essential for interpreting superconducting STM measurements and characteristics of other superconducting devices with small tunnel junctions, such as qubits [30, 56–58].

VII. ACKNOWLEDGMENTS

We thank D. Averin for fruitful discussions and providing the MAR code for the symmetric junction, as well as Z. Steffen and B. S. Palmer for offering useful insights on the MAR calculations. We acknowledge support from the Laboratory for Physical Sciences, the JQI, CNAM, and from the NSF for supporting development of the STM under grant

- [1] B. Josephson, Physics Letters **1**, 251 (1962).
- [2] E. Scheer, N. Agraït, J. C. Cuevas, A. L. Yeyati, B. Ludoph, A. Martín-Rodero, G. R. Bollinger, J. M. van Ruitenbeek, and C. Urbina, Nature **394**, 154 (1998).
- [3] N. Agrait, J. G. Rodrigo, and S. Vieira, Phys. Rev. B **46**, 5814 (1992).
- [4] J. G. Rodrigo, H. Suderow, S. Vieira, E. Bascones, and F. Guinea, J. Phys.: Condens. Matter **16**, R1151 (2004).
- [5] I. Guillamon, H. Suderow, S. Vieira, and P. Rodiere, Physica C **468**, 537 (2008).
- [6] J. G. Rodrigo, V. Crespo, and S. Vieira, Physica C **437**, 270 (2006).
- [7] D. Averin and A. Bardas, Phys. Rev. lett. **75**, 1831 (1995).
- [8] J. C. Cuevas, A. Martin-Rodero, and A. L. Yeyati, Phys. Rev. B **54**, 7366 (1996).
- [9] C. J. Muller, J. M. van Ruitenbeek, and L. J. de Jongh, Physica C **191**, 485 (1992).
- [10] E. Scheer, P. Joyez, D. Esteve, C. Urbina, and M. H. Devoret, Phys. Rev. Lett. **78**, 3535 (1997).
- [11] M. Ternes, W.-D. Schneider, J.-C. Cuevas, C. P. Lutz, C. F. Hirjibehedin, and A. J. Heinrich, Phys. Rev. B **74**, 132501 (2006).
- [12] N. Agrait, A. L. Yeyati, and J. M. Van Ruitenbeek, Phys. Reports **377**, 81 (2003).
- [13] R. Hiraoka, R. Arafune, N. Tsukahara, M. Kawai, and N. Takagi, Phys. Rev. B **90**, 241405 (2014).
- [14] H. Kimura, R. P. Barber, S. Ono, Y. Ando, and R. C. Dynes, Phys. Rev. Lett. **101**, 037002 (2008).
- [15] M. H. Hamidian, S. D. Edkins, S. H. Joo, A. Kostin, H. Eisaki, S. Uchida, M. J. Lawler, E.-A. Kim, A. P. Mackenzie, K. Fujita, and J. C. S. Davis, Nature **532**, 343 (2016).
- [16] M. T. Randeria, B. E. Feldman, I. K. Drozdov, and A. Yazdani, Phys. Rev. B **93**, 161115 (2016).
- [17] C. R. Ast, B. Jäck, J. Senkpiel, M. Eltschka, M. Etzkorn, J. Ankerhold, and K. Kern, Nature communications **7**, 13009 (2016).
- [18] B. Jäck, M. Eltschka, M. Assig, M. Etzkorn, C. R. Ast, and K. Kern, Phys. Rev. B **93**, 020504 (2016).

[19] B. Jäck, J. Senkpiel, M. Etzkorn, J. Ankerhold, C. R. Ast, and K. Kern, Phys. Rev. Lett. **119**, 147702 (2017).

[20] J. Senkpiel, S. Dambach, M. Etzkorn, R. Drost, C. Padurariu, B. Kubala, W. Belzig, A. L. Yeyati, J. C. Cuevas, J. Ankerhold, C. R. Ast, and K. Kern, Communications Physics **3**, 131 (2020).

[21] J. Senkpiel, J. C. Klöckner, M. Etzkorn, S. Dambach, B. Kubala, W. Belzig, A. L. Yeyati, J. C. Cuevas, F. Pauly, J. Ankerhold, C. R. Ast, and K. Kern, Phys. Rev. Lett. **124**, 156803 (2020).

[22] M. Uhl, P. Kot, R. Drost, H. Huang, J. Ankerhold, J. C. Cuevas, and C. R. Ast, Phys. Rev. Res. **6**, 043233 (2024).

[23] M. Graham and D. K. Morr, Phys. Rev. Lett. **123**, 017001 (2019).

[24] A. Roychowdhury, M. Dreyer, J. R. Anderson, C. J. Lobb, and F. C. Wellstood, Phys. Rev. Appl. **4**, 034011 (2015).

[25] Z. Steffen, S. K. Dutta, H. Wang, K. Li, Y. Huang, Y.-H. Huang, A. Mathur, F. C. Wellstood, and B. S. Palmer, IEEE Transactions on Applied Superconductivity **33**, 1 (2023).

[26] A. Roychowdhury, M. A. Gubrud, R. Dana, J. R. Anderson, C. J. Lobb, F. C. Wellstood, and M. Dreyer, Rev. Sci. Instrum. **85**, 043706 (2014).

[27] T. Proslie, A. Kohen, Y. Noat, T. Cren, D. Roditchev, and W. Sacks, Europhys. Lett. **73**, 962 (2006).

[28] N. Bergeal, Y. Noat, T. Cren, T. Proslie, V. Dubost, F. Debontiridder, A. Zimmers, D. Roditchev, W. Sacks, and J. Marcus, Phys. Rev. B **78**, 140507 (2008).

[29] M. Trahms, L. Melischek, J. F. Steiner, B. Mahendru, I. Tamir, N. Bogdanoff, O. Peters, G. Reecht, C. B. Winkelmann, F. von Oppen, and K. J. Franke, Nature **615**, 628 (2023).

[30] W.-S. Lu, K. Kalashnikov, P. Kamenov, T. J. DiNapoli, and M. E. Gershenson, Electronics **12**, 416 (2023).

[31] S.-T. Wu and S. Yip, Phys. Rev. B **70**, 104511 (2004).

[32] See Supplemental Material at [] for details on the MAR theory, experimental measurements, and data analysis [59–61].

[33] W.-T. Liao, University of Maryland, Ph.D. Dissertation (2019).

[34] V. Ambegaokar and A. Baratoff, Phys. Rev. Lett. **10**, 486 (1963).

[35] D. F. Sullivan, S. K. Dutta, M. Dreyer, M. A. Gubrud, A. Roychowdhury, J. R. Anderson, C. J. Lobb, and F. C. Wellstood, *J. Appl. Phys.* **113**, 183905 (2013).

[36] A. Roychowdhury, R. Dana, M. Dreyer, J. R. Anderson, C. J. Lobb, and F. C. Wellstood, *J. Appl. Phys.* **116**, 014308 (2014).

[37] Nb (100) single crystal, Accument Materials, USA.

[38] E. Scheer, W. Belzig, Y. Naveh, M. H. Devoret, D. Esteve, and C. Urbina, *Phys. Rev. Lett.* **86**, 284 (2001).

[39] B. Ludolph, N. Van der Post, E. N. Bratus, E. V. Bezuglyi, V. S. Shumeiko, G. Wendin, and J. M. van Ruitenbeek, *Phys. Rev. B* **61**, 8561 (2000).

[40] C. C. Koch, J. O. Scarbrough, and D. M. Kroeger, *Phys. Rev. B* **9**, 888 (1974).

[41] T. P. Orlando and K. A. Delin, *Foundations of applied superconductivity* (Addison-Wesley, 1991).

[42] M. Tinkham, *Introduction to Superconductivity* (Courier Dover Publications, 2012).

[43] Y. C. Chen, M. P. A. Fisher, and A. J. Leggett, *J. Appl. Phys.* **64**, 3119 (1988).

[44] S. Kurokawa and A. Sakai, *Science reports of the Research Institutes, Tohoku University. Ser. A, Physics, chemistry and metallurgy* **44**, 173 (1997).

[45] J. M. de Voogd, M. A. van Spronsen, F. E. Kalff, B. Bryant, O. Ostojić, A. M. J. den Haan, I. M. N. Groot, T. H. Oosterkamp, A. F. Otte, and M. J. Rost, *Ultramicroscopy* **181**, 61 (2017).

[46] S. Kurokawa and A. Sakai, *J. Appl. Phys.* **83**, 7416 (1998).

[47] M. Iansiti, M. Tinkham, A. T. Johnson, W. F. Smith, and C. J. Lobb, *Phys. Rev. B* **39**, 6465 (1989).

[48] M. H. Devoret, J. M. Martinis, and J. Clarke, *Phys. Rev. Lett.* **55**, 1908 (1985).

[49] J. M. Martinis, M. H. Devoret, and J. Clarke, *Phys. Rev. B* **35**, 4682 (1987).

[50] Y. M. I. Anchenko and L. A. Zil'berman, *Sov. Phys. JETP* **28**, 113 (1969).

[51] M. H. Devoret, J. M. Martinis, D. Esteve, and J. Clarke, *Phys. Rev. Lett.* **53**, 1260 (1984).

[52] G.-L. Ingold, H. Grabert, and U. Eberhardt, *Phys. Rev. B* **50**, 395 (1994).

[53] W.-T. Liao, C. J. Lobb, F. C. Wellstood, and M. Dreyer, *J. Appl. Phys.* **121**, 214501 (2017).

[54] D. J. van Harlingen, *Physica C* **282**, 128 (1997).

[55] D. J. van Harlingen, J. E. Hilliard, B. L. T. Plourde, and B. D. Yanoff, *Physica C* **317-318**, 410 (1999).

- [56] J. Ridderbos, M. Brauns, A. Li, E. P. Bakkers, A. Brinkman, W. G. Van Der Wiel, and F. A. Zwanenburg, Phys. Rev. Materials **3**, 084803 (2019).
- [57] M. Hays, G. de Lange, K. Serniak, D. J. van Woerkom, D. Bouman, P. Krogstrup, J. Nygård, A. Geresdi, and M. H. Devoret, Phys. Rev. Lett. **121**, 047001 (2018).
- [58] L. Tosi, C. Metzger, M. F. Goffman, C. Urbina, H. Pothier, S. Park, A. L. Yeyati, J. Nygård, and P. Krogstrup, Phys. Rev. X **9**, 011010 (2019).
- [59] J. P. Pekola, J. V. Koski, and D. V. Averin, Phys. Rev. B **89**, 081309 (2014).
- [60] J. T. Muhonen, M. Meschke, and J. P. Pekola, Rep. Prog. Phys. **75**, 046501 (2012).
- [61] F. Giavotto, T. T. Heikkilä, A. Luukanen, A. M. Savin, and J. P. Pekola, Rev. Mod. Phys. **78**, 217 (2006).

TABLE I. Extracted parameters of the normal state tunneling resistance R_n , superconducting energy gaps Δ_s and Δ_t , transparency D , and effective number of channels N , for the $V(I)$ characteristics in Fig. 7

R_n (k Ω)	Δ_s (meV)	Δ_t (meV)	D	N
57	1.497	0.670	0.1	2.26
7.9	1.486	0.627	0.27	6.05
1.08	1.479	0.579	0.6	19.91

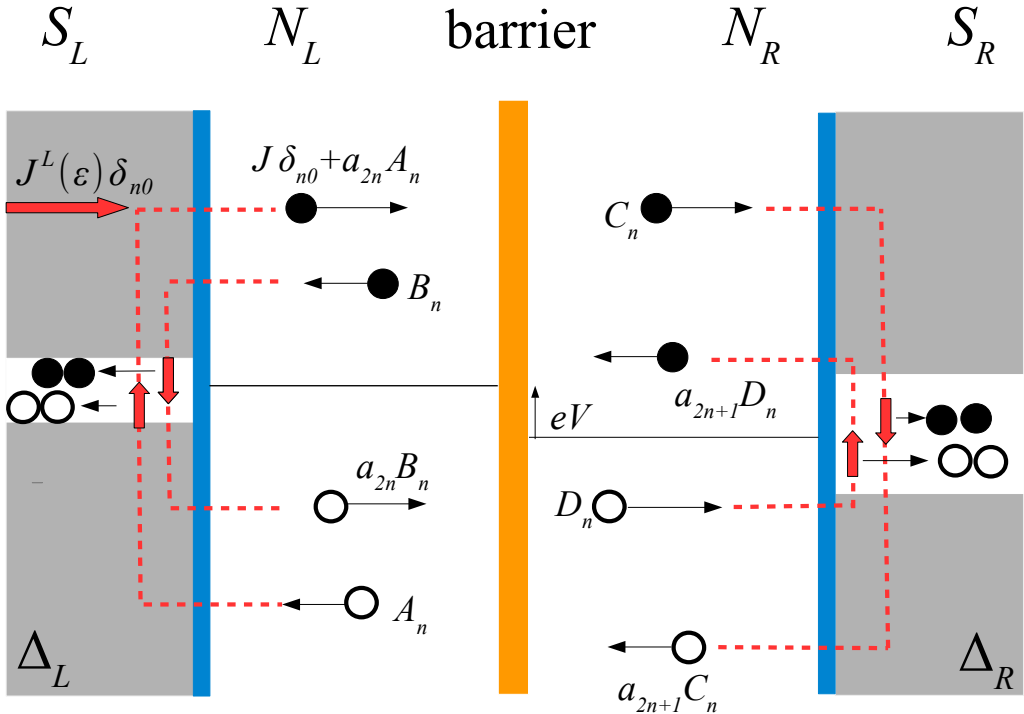


FIG. 1. Illustration showing MAR wavefunction components of the generalized AB model for the case of electron-like source quasiparticles incident from the left. The left lead is a superconductor with gap Δ_L and the right lead is a superconductor with gap Δ_R . A voltage bias V is applied to the right lead with respect to the left lead. The barrier in the center acts as a scattering region for quasiparticles and is characterized by transparency D (distinct from the incident hole term D_n). The superconductor-to-normal metal interfaces (blue) have unity transparency.

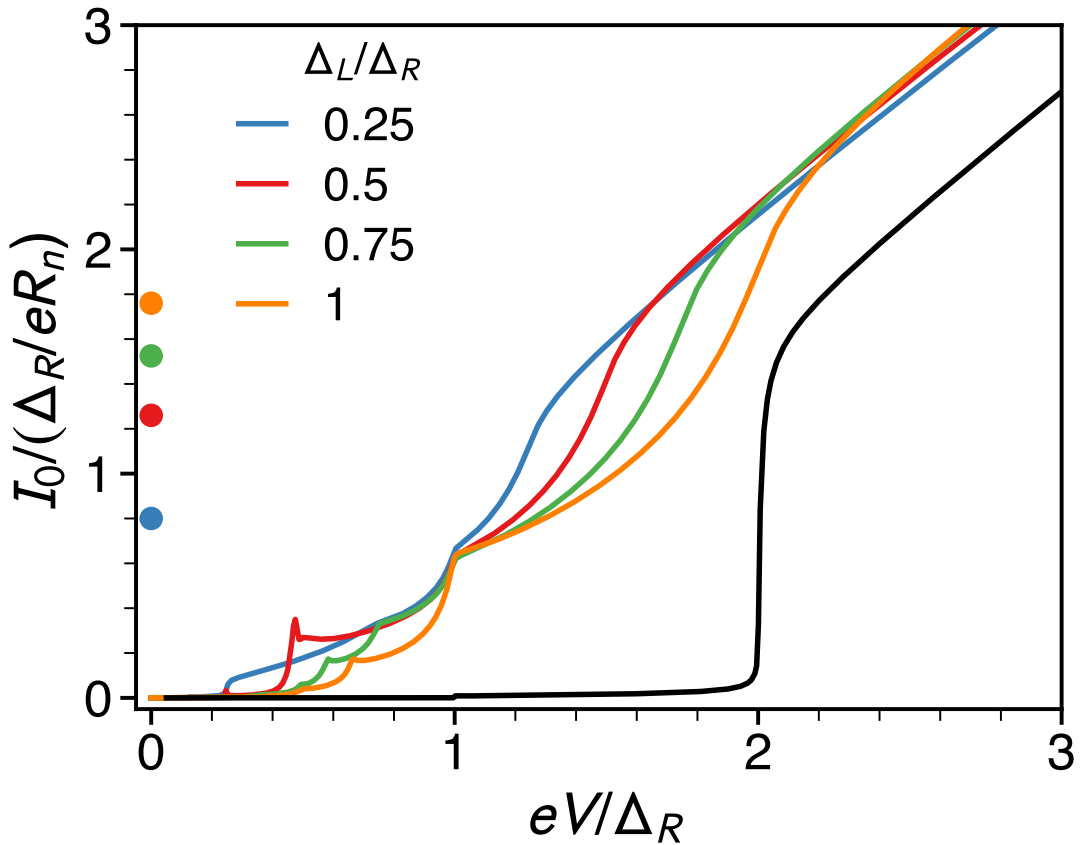


FIG. 2. $I - V$ characteristics for superconducting gap ratios $\Delta_L/\Delta_R = 0.25$ (blue), 0.5 (red), 0.75 (green) and 1 (orange) at transparency $D = 0.4$ for $T = 0$ K. Circles at $V = 0$ show corresponding critical currents from Eq. (12). For comparison, also shown is the $I - V$ curve for a symmetric junction with $D = 0.01$ (black), near the conventional tunnel limit.

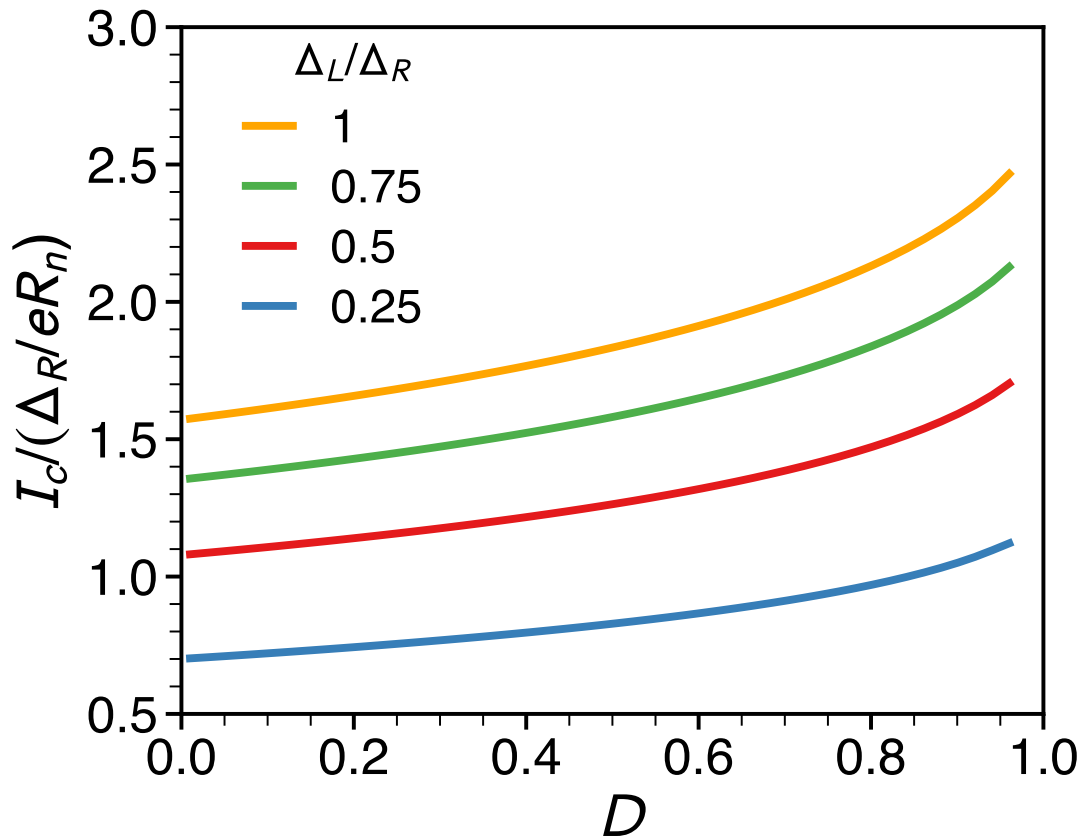


FIG. 3. Normalized critical current as a function of D for $\Delta_L / \Delta_R = 0.25$ (blue), 0.5 (red), 0.75 (green) and 1 (orange) at $T = 0$ K.

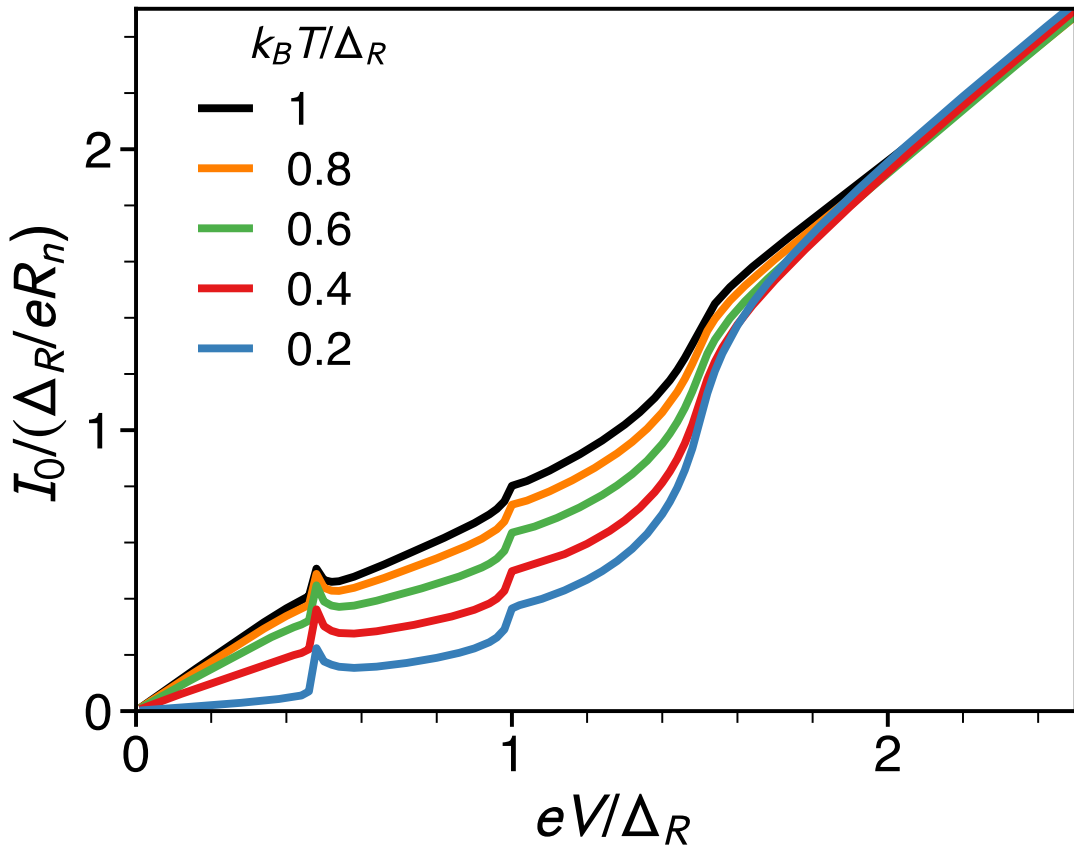


FIG. 4. Effects of temperature on calculated $I - V$ characteristics for transparency $D = 0.25$ and $\Delta_L/\Delta_R = 0.5$. The curves correspond to $k_B T/\Delta_R$ values of 1 (black), 0.8 (orange), 0.6 (green), 0.4 (red), and 0.2 (blue).

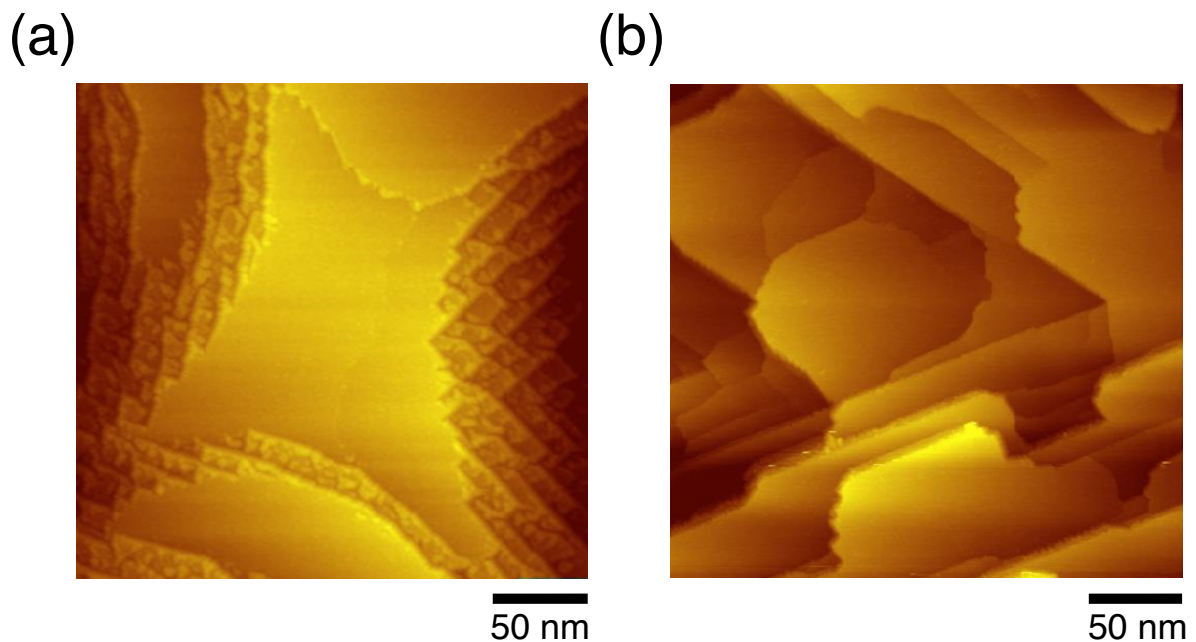


FIG. 5. Topography of representative regions on the Nb(100) crystal surface obtained using a Nb STM tip at (a) 1.5 K and (b) 50 mK. Image (b) shows atomically flat regions with single layer steps of about 0.3 nm.

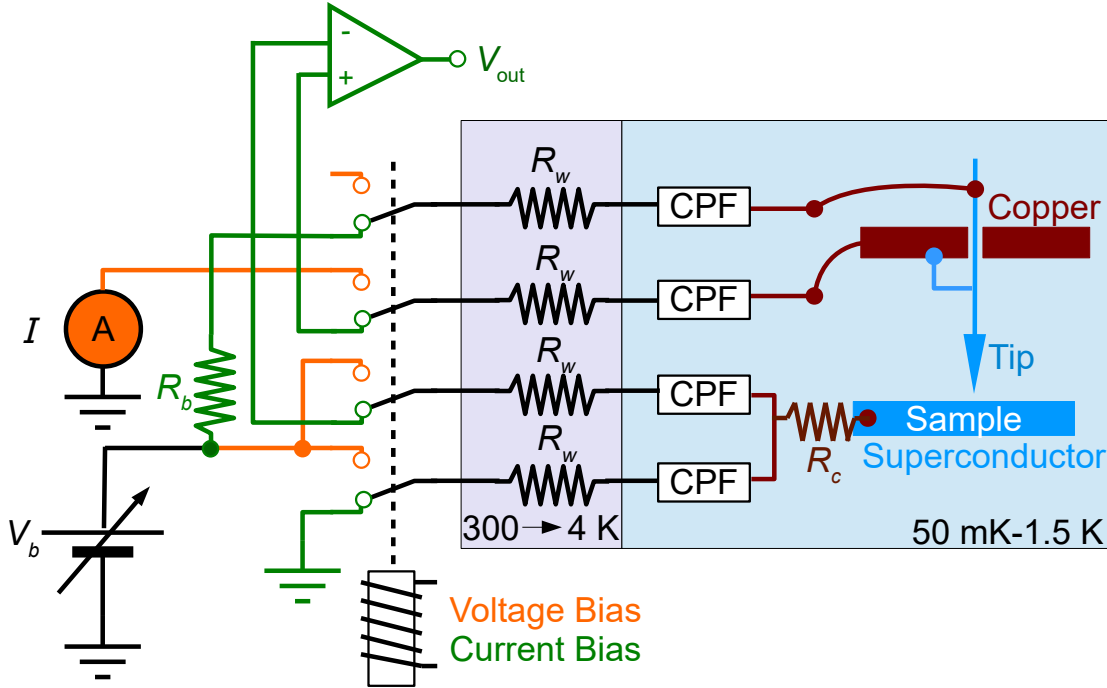


FIG. 6. Measurement schematic, including the relay box used to switch from voltage-biased mode to current-biased mode. The bias resistor R_b is set to 1, 10, or $100 \text{ M}\Omega$, depending on the tunnel junction resistance. $R_w \approx 220 \Omega$ is the resistance of each line in the refrigerator and R_c is the contact resistance between the sample mounting stud and the measurement wires. The copper powder filters (CPF) are used to filter out high frequency noise.

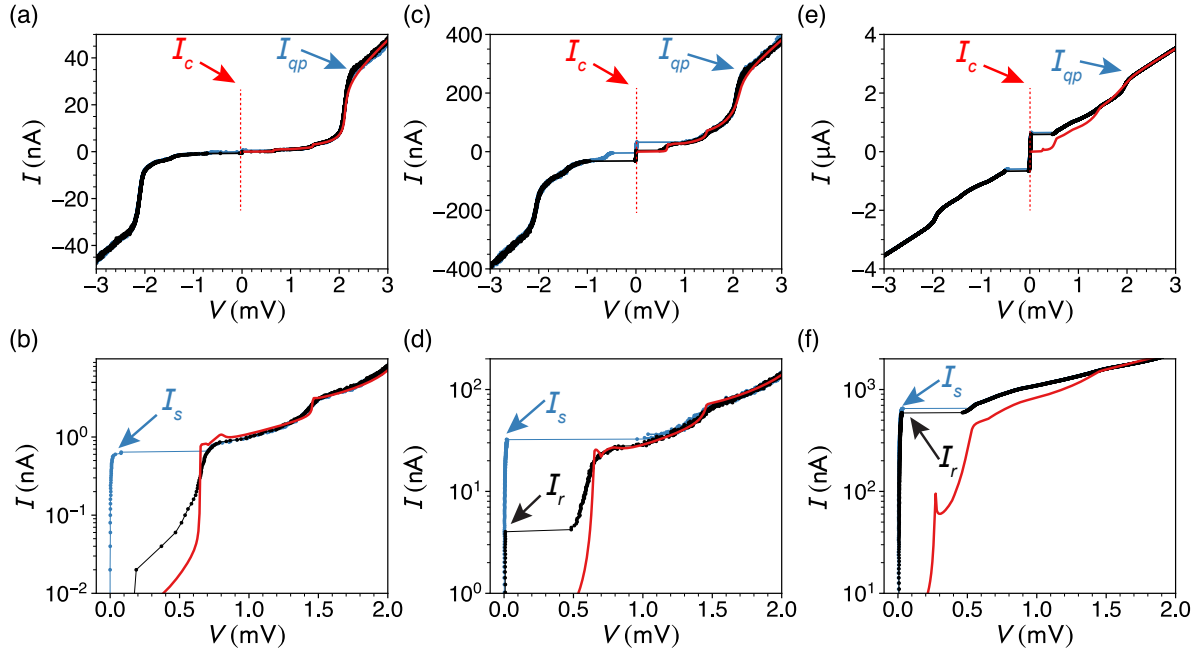


FIG. 7. $V(I)$ characteristics for junction tunneling resistance R_n of (a) and (b) $57 \text{ k}\Omega$, (c) and (d) $7.9 \text{ k}\Omega$, and (e) and (f) $1.08 \text{ k}\Omega$. Linear plots are shown in the first row, while the second row shows semilog graphs, revealing details of the switching and the retrapping behaviors. Each panel shows forward (blue) and reverse (black) sweeps measured at 1.5 K , along with a fit curve from the asymmetric MAR theory of Eq. (13) (red solid line). Also shown is the ideal supercurrent branch at zero voltage (red dashed line), which ends at the critical current I_c , predicted from MAR theory. See Table I for fit parameters.

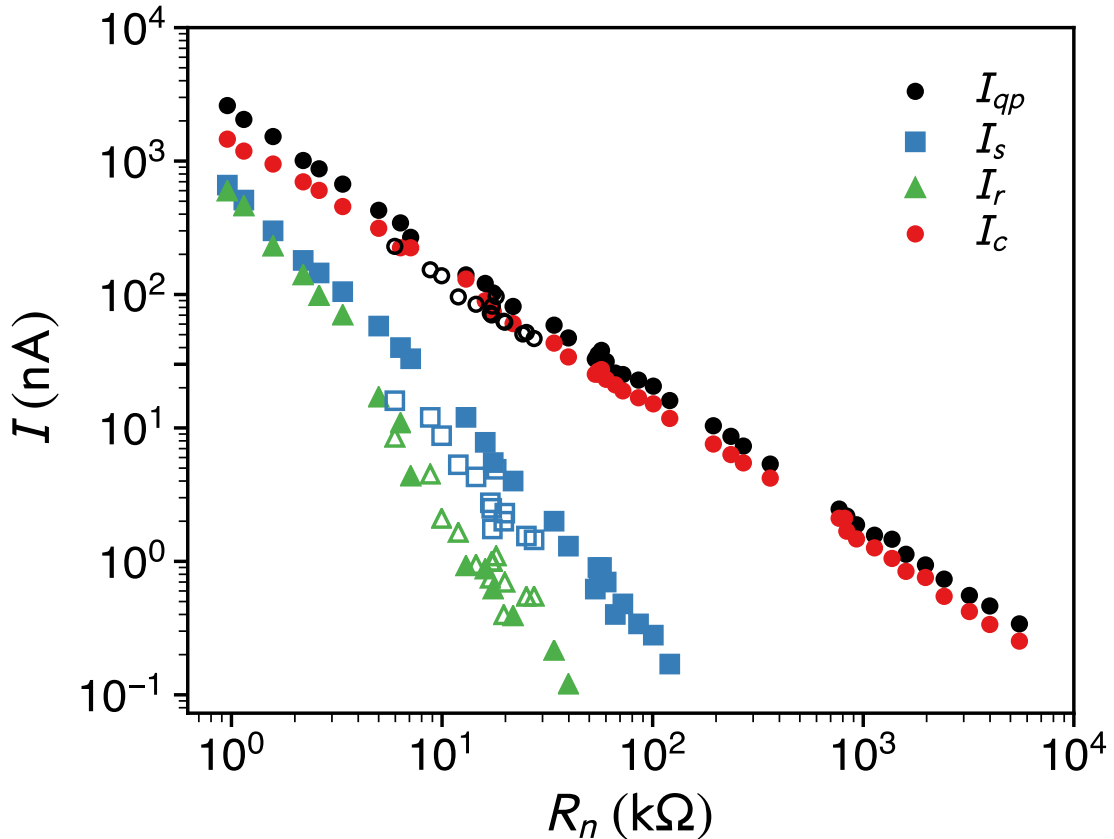


FIG. 8. Extracted quasiparticle current I_{qp} (black circles), switching current I_s (blue squares), and retrapping current I_r (green triangles) as a function of R_n , for data acquired at 50 mK (open symbols) and 1.5 K (filled). The theoretical critical current I_c (red) was calculated from the asymmetric MAR theory using the fitted parameters R_n , Δ_s , Δ_t , and D for each curve. For $R_n > 105$ kΩ, there was no observed supercurrent branch, so I_s and I_r could not be determined. For $R_n < 3$ kΩ, hysteretic behavior disappeared.

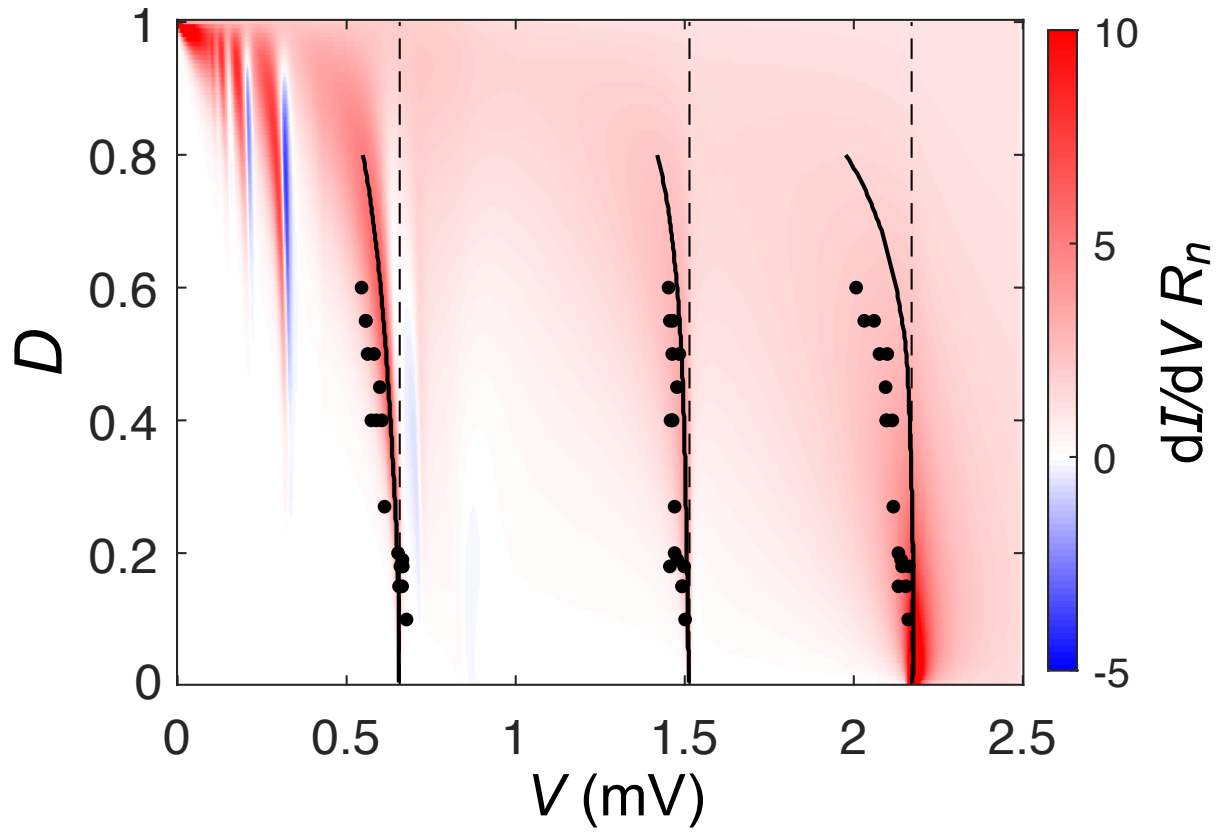


FIG. 9. dI/dV peak locations V_t , V_s , and V_{st} (black circles) extracted from the data, on top of theoretical values of dI/dV (pseudocolor plot), normalized by R_n , for $\Delta_t = 0.657$ meV and $\Delta_s = 1.514$ meV at $T = 1.5$ K. The peaks extracted from the theory (solid curve) deviate from the fixed gaps (dashed) with increasing transparency.

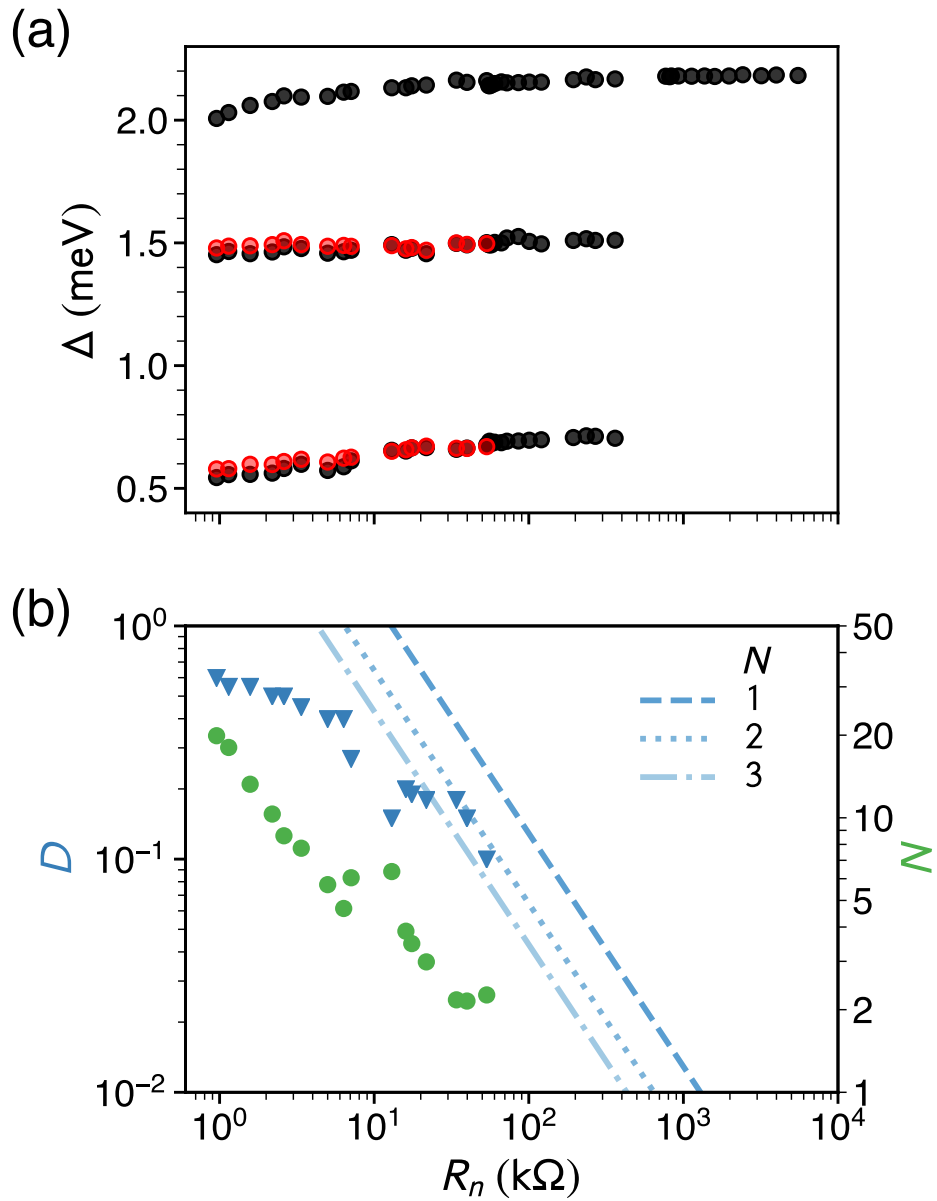


FIG. 10. (a) Black circles are the peaks eV_s , eV_t , and eV_{st} , as a function of R_n , extracted from the experimental dI/dV data. Red circles show Δ_s , Δ_t as a function of R_n , fitted from the asymmetric MAR theory by minimizing the difference between the theoretical dI/dV peaks and the measured dI/dV peaks. (b) Log-log plot of the extracted transparency D (blue triangles) and effective number of channels N (green circles) as a function of R_n , from fitting the asymmetric MAR theory to $V(I)$ curves. The dashed lines are the theoretical transparency D as a function of junction resistance R_n for fixed values of N .

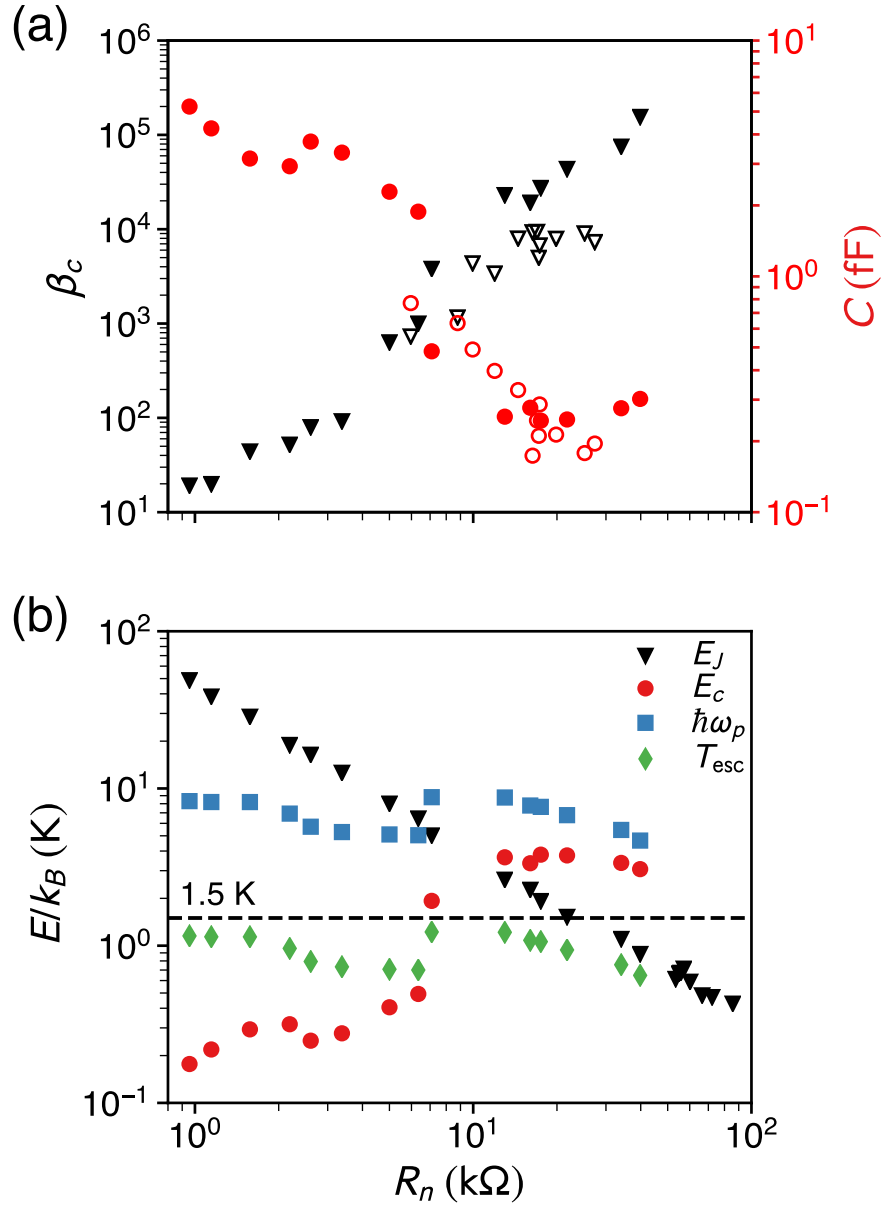


FIG. 11. (a) Extracted values of the Stewart-McCumber parameter β_c (black triangles) and the total effective capacitance C (red circles) of the junction versus tunneling resistance R_n , for data acquired at 50 mK (open symbols) and 1.5 K (filled). (b) Josephson energy E_J (black triangles), charging energy E_c (red circles) and plasma energy $\hbar\omega_p$ (blue squares) versus normal resistance R_n of the junction. The green diamonds show the MQT escape temperature T_{esc} . The higher temperature at which data were acquired is shown for reference (dashed line).

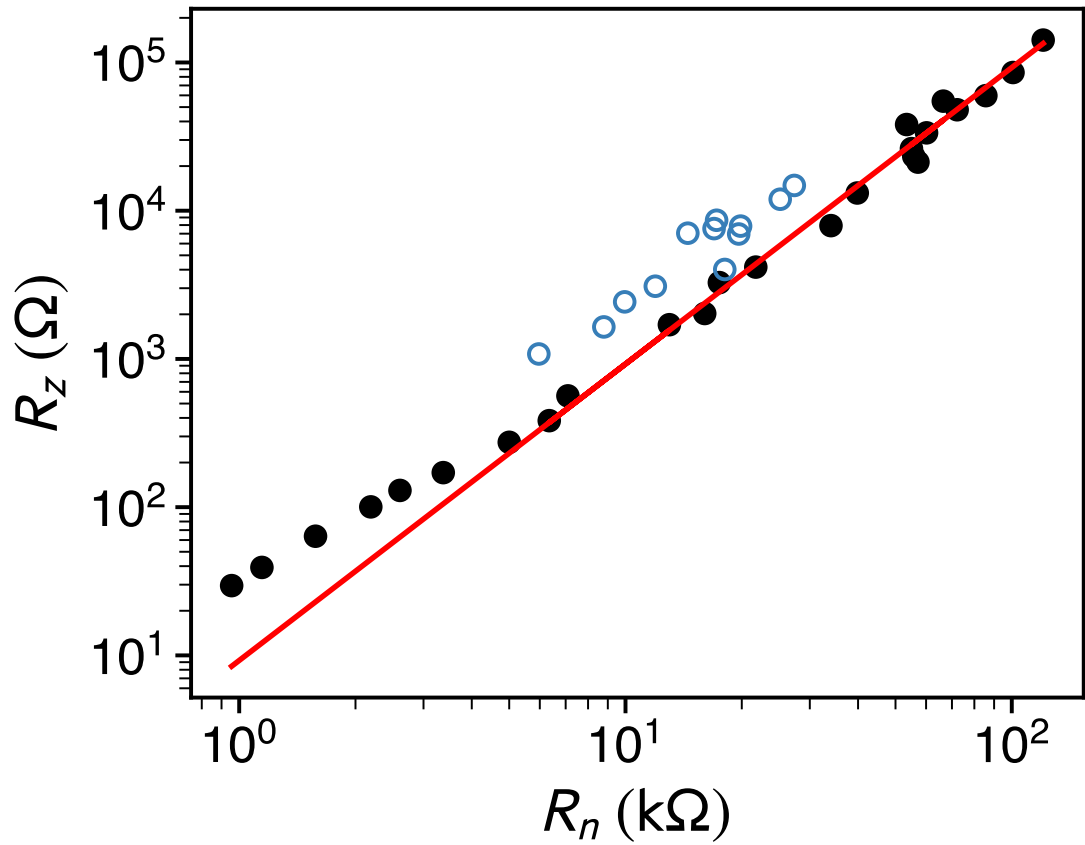


FIG. 12. Resistance of the supercurrent branch R_z versus tunnel resistance R_n of the junction. The values extracted from measurements at 50 mK (open blue circles) and 1.5 K (black circles) roughly scale as $R_z \propto R_n^2$ (red).

SUPPLEMENTAL MATERIAL

Appendix A: Multiple Andreev Reflection

In Fig. 1 of the main text, the schematic drawing of the Andreev process only shows the wavefunction components for the left and the right superconductor. Here, we show example trajectories for an electron-like source quasiparticle incident from the left superconductor. Note that the superconducting gap is different between the left and the right superconductors. The voltage bias V is applied to the right superconducting electrode S_R with respect to the left superconducting electrode S_L .

An electron-like source quasiparticle incident from the left superconductor with energy ε will travel to the right interface barrier due to the applied voltage V , it goes through the center barrier, with partial backward reflection, and partial forward transmission. When it reaches the right superconductor, the electron-like quasiparticle has picked up energy eV , resulting in an energy $(\varepsilon + eV)$. At the right interface $N_R - S_R$, it goes through the Andreev reflection process with amplitude $a^R(\varepsilon + eV)$ and emerges as a hole-like quasiparticle with energy $-(\varepsilon + eV)$.

The hole-like quasiparticle will then travel towards the left electrode. It encounters the barrier again, resulting in partial transmission and partial reflection. The transmitted hole-like quasiparticle travels back to the left interface $N_L - S_L$, picking up extra energy eV , becoming $-(\varepsilon + 2eV)$. At the interface $N_L - S_L$, the hole-like quasiparticle is again Andreev reflected back as electron-like quasiparticle, with energy $\varepsilon + 2eV$. This process continues, allowing the iterative construction of the electron and hole wavefunctions in the normal regions.

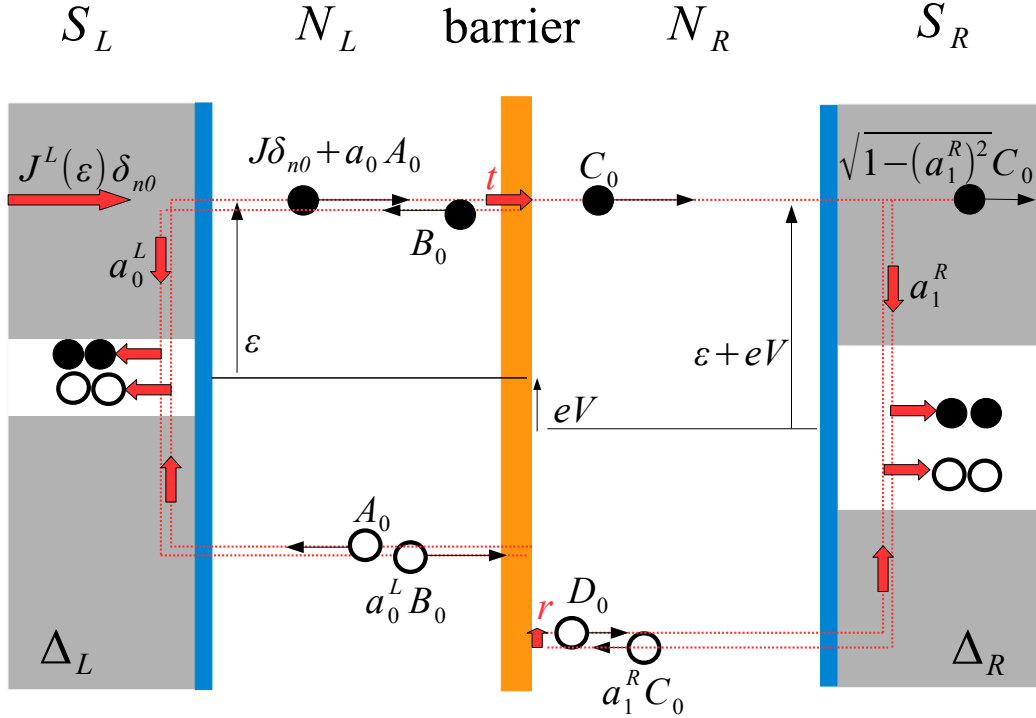


FIG. S.1. Illustration showing MAR in the generalized AB model for the case of electron-like source quasiparticles incident from the left. The barrier (orange) in the center acts as a scattering region for quasiparticles and is characterized by transparency D (distinct from the incident hole term D_n). The superconductor-to-normal metal interfaces (blue) have unity transparency. The wavefunction amplitudes C_n , and D_n at the right interface are shown. The superscript in A_n , B_n , C_n , D_n is not labeled here for ease of visualizing the complex process.

Appendix B: MAR wavefunctions for a quasiparticle incident from the right

In Eqs. (3) and (4) of the main text, we listed the final electron and hole wavefunctions for an electron-like quasiparticle incident from the left and a hole-like quasiparticle incident from the left. Here we write down the wavefunctions for an electron-like quasiparticle incident from the right, and a hole-like quasiparticle incident from the right. For consistency, k is the Fermi wavevector associated with the quasiparticle at energy ε , positive by definition. Thus an electron traveling to the right has the same value of k as a hole traveling to the left.

The wavefunctions in the normal region for an electron-like quasiparticle incident from the right when $D \neq 1$ are

$$\begin{aligned}\psi_e^{eR} &= \sum_{n=-\infty}^{\infty} [(a_{\{2n,-\}}^R A_n^{\leftarrow} + J^R \delta_{n0}) e^{-ikx} + B_n^{\leftarrow} e^{+ikx}] e^{-i(\varepsilon-2neV)t/\hbar} \\ \psi_h^{eR} &= \sum_{n=-\infty}^{\infty} [A_n^{\leftarrow} e^{-ikx} + a_{\{2n,-\}}^R B_n^{\leftarrow} e^{+ikx}] e^{-i(\varepsilon-2neV)t/\hbar},\end{aligned}\quad (\text{S1})$$

where $a_{\{2n,-\}}^R = a^R(\varepsilon - 2neV)$ and $J^R(\varepsilon) = \sqrt{[1 - |a^R(\varepsilon)|^2]}$.

The wavefunctions in the normal region for a hole-like quasiparticle incident from the right are

$$\begin{aligned}\psi_h^{hR} &= \sum_{n=-\infty}^{\infty} [(a_{\{2n,+}\}^R A_n^{\leftarrow} + J^R \delta_{n0}) e^{+ikx} + B_n^{\leftarrow} e^{-ikx}] e^{-i(\varepsilon+2neV)t/\hbar} \\ \psi_e^{hR} &= \sum_{n=-\infty}^{\infty} [A_n^{\leftarrow} e^{+ikx} + a_{\{2n,+}\}^R B_n^{\leftarrow} e^{-ikx}] e^{-i(\varepsilon+2neV)t/\hbar},\end{aligned}\quad (\text{S2})$$

where $a_{\{2n,+}\}^R = a^R(\varepsilon + 2neV)$. For electron-like and hole-like source quasiparticles incident from the right, the amplitudes are labeled as A_n^{\leftarrow} and B_n^{\leftarrow} .

The total probability current density is then

$$\begin{aligned}j_R &= \frac{\hbar}{2mi} [(\psi_e^{eR*} \nabla \psi_e^{eR} - \psi_e^{eR} \nabla \psi_e^{eR*}) + (\psi_h^{eR*} \nabla \psi_h^{eR} - \psi_h^{eR} \nabla \psi_h^{eR*})] \\ &\quad + \frac{\hbar}{2mi} [(\psi_e^{hR*} \nabla \psi_e^{hR} - \psi_e^{hR} \nabla \psi_e^{hR*}) + (\psi_h^{hR*} \nabla \psi_h^{hR} - \psi_h^{hR} \nabla \psi_h^{hR*})].\end{aligned}\quad (\text{S3})$$

The total electrical current due to an electron and hole incident from the right is directly proportional to the electron probability current density. Summing over the source energies,

$$I_R(t) = \frac{e}{2\pi\hbar} \frac{m}{\hbar k} \int_{-\infty}^{\infty} d\varepsilon j_R(\varepsilon, t) f(\varepsilon), \quad (\text{S4})$$

where $f(\varepsilon) = (e^{\varepsilon/k_B T} + 1)^{-1}$ is the electron occupancy for states at energy ε , which we assume is a Fermi distribution.

Appendix C: Recursion Relation derivation

The recursion relations are introduced solely to eliminate the degrees of freedom of the left normal region by connecting the right normal region through the normal-state scattering matrix; as a result, their form is independent of the asymmetry of the superconducting gaps and remains identical to the symmetric-gap case. For simplicity, we will assume the superconducting gaps of the left and right electrode are the same in this section, and will omit the \rightarrow in the wavefunctions.

The wavefunctions in region N_L produced by an electron-like quasiparticle incident from the left can be written as [7]

$$\begin{aligned} \psi_e &= \sum_n [(a_{2n}A_n + J\delta_{n0})e^{ikx} + B_n e^{-ikx}] e^{-i(\varepsilon+2neV)t/\hbar} \\ \psi_h &= \sum_n [A_n e^{ikx} + a_{2n}B_n e^{-ikx}] e^{-i(\varepsilon+2neV)t/\hbar}. \end{aligned} \quad (\text{S1})$$

The wavefunctions in region N_R produced by an electron-like quasiparticle incident from the left can be written as

$$\begin{aligned} \psi_e &= \sum_n [C_n e^{ikx} + a_{2n+1}D_n e^{-ikx}] e^{-i(\varepsilon+(2n+1)eV)t/\hbar} \\ \psi_h &= \sum_n [a_{2n+1}C_n e^{ikx} + D_n e^{-ikx}] e^{-i(\varepsilon+(2n+1)eV)t/\hbar}, \end{aligned} \quad (\text{S2})$$

where the sum over n represents contributions from multiple reflections and is taken over all integers from $-\infty$ to ∞ .

We can relate the incoming electrons to the outgoing electrons in regions N_L and N_R using a scattering matrix S_e . Similarly there will be a scattering matrix S_h connecting the

holes in the two regions:

$$\begin{pmatrix} B_n \\ C_n \end{pmatrix} = S_e \begin{pmatrix} a_{2n}A_n + J\delta_{n0} \\ a_{2n+1}D_n \end{pmatrix}, \quad \begin{pmatrix} A_n \\ D_{n-1} \end{pmatrix} = S_h \begin{pmatrix} a_{2n}B_n \\ a_{2n-1}C_{n-1} \end{pmatrix} \quad (S3)$$

The scattering matrices that represent the barrier for the electrons S_e and holes S_h are [7]

$$S_h = S_e^*, \quad S_e = \begin{pmatrix} r & t \\ t & -r^*t/t^* \end{pmatrix}, \quad (S4)$$

where r is the amplitude of the quasiparticle being reflected in the normal region, and t is the amplitude of the quasiparticle being transmitted in the normal region. Here the transparency is $D = |t|^2$.

Eliminating the wavefunction amplitudes C_n and D_n in N_R using Eq. (S3) and Eq. (S4), the recursion relation for the amplitudes A_n and B_n will be

$$A_{n+1} - a_{2n+1}a_{2n}A_n = \sqrt{R}(a_{2n+2}B_{n+1} - a_{2n+1}B_n) + Ja_1\delta_{n0} \quad (S5)$$

$$\begin{aligned} D \frac{a_{2n+1}a_{2n+2}}{1 - (a_{2n+1})^2} B_{n+1} - \left[D \left(\frac{(a_{2n+1})^2}{1 - (a_{2n+1})^2} + \frac{(a_{2n})^2}{1 - (a_{2n-1})^2} \right) + 1 - (a_{2n})^2 \right] B_n \\ + D \frac{a_{2n}a_{2n-1}}{1 - a_{2n-1}} B_{n-1} = -\sqrt{R}J\delta_{n,0}, \end{aligned} \quad (S6)$$

with a detailed derivation given in Ref [33].

In the wavefunctions coefficients A_n^\rightarrow , B_n^\rightarrow , C_n^\rightarrow , D_n^\rightarrow , the symbol \rightarrow is used to discern an electron-like quasiparticle incident from the left as opposed to an electron-like quasiparticle incident from the right. To properly keep track of the left or the right interface where it is Andreev reflected from a quasiparticle incident from the right or left, we write superscript A^\rightarrow , B^\rightarrow , A^\leftarrow , B^\leftarrow , and label the Andreev reflection according to the interface. The recursion relations for A^\rightarrow , B^\rightarrow are Eqs. 10 and 11 in the main text while the resulting recursion relations for A^\leftarrow , B^\leftarrow are

$$A_{n+1}^\leftarrow - a_{2n+1}^L a_{2n}^R A_n^\leftarrow = \sqrt{R}(a_{2n+2}^R B_{n+1}^\leftarrow - a_{2n+1}^L B_n^\leftarrow) + J^R a_1^L \delta_{n0} \quad (S7)$$

$$\begin{aligned} D \frac{a_{2n+1}^L a_{2n+2}^R}{1 - (a_{2n+1}^L)^2} B_{n+1}^\leftarrow - \left[D \left(\frac{(a_{2n+1}^L)^2}{1 - (a_{2n+1}^L)^2} + \frac{(a_{2n}^R)^2}{1 - (a_{2n-1}^L)^2} \right) + 1 - (a_{2n}^R)^2 \right] B_n^\leftarrow \\ + D \frac{a_{2n}^R a_{2n-1}^L}{1 - a_{2n-1}^L} B_{n-1}^\leftarrow = -\sqrt{R}J^R \delta_{n0}. \end{aligned} \quad (S8)$$

We see that the recursion relations for A^{\leftarrow} , B^{\leftarrow} are identical to A^{\rightarrow} , B^{\rightarrow} simply by substituting superscripts \rightarrow for \leftarrow , L for R , and R for L .

Appendix D: Subgap current for different electrode temperatures

In Fig. 4 of the main paper, theoretical $I - V$ characteristics are plotted for different temperatures. While both electrodes of a junction are often at the same temperature, situations where there is a temperature difference are also of interest. Asymmetric junctions in temperature have been used as electronic refrigerators [59–61]. Thermal transport and heating effects can be important in small junctions. For the current work, the sharpened STM tip may have more difficulty dissipating heat and thus reach a higher temperature than the superconducting sample. We can simulate the effect of this by independently specifying the temperatures T_L and T_R on the left and right sides of the junction.

Figure S.2 shows dc $I - V$ characteristics for four different scenarios. For all the curves, we set the superconducting gap ratio to $\Delta_L/\Delta_R = 0.5$, the transparency to $D = 0.25$, and $\Delta_R = 1$ meV. The black line corresponds to both sides of the junction at 0.06 K, while the blue line shows $T_L = T_R = 2.3$ K. For the higher temperature, the MAR steps occur at the same voltages, but the subgap currents are larger due to a larger population of thermally excited quasiparticles. The other two cases correspond to a temperature difference: the red dashed line shows $T_L = 0.06$ K and $T_R = 2.3$ K, while the orange dashed line is for $T_L = 2.3$ K and $T_R = 0.06$ K. Comparing the four curves shows that the behavior of the $I - V$ curve is largely governed by the temperature of the electrode with the larger superconducting gap (T_R , in this example). Thus, for the data presented in the main text, we suspect the $I - V$ curves are more strongly influenced by the temperature of the sample, which had a larger gap than the tip.

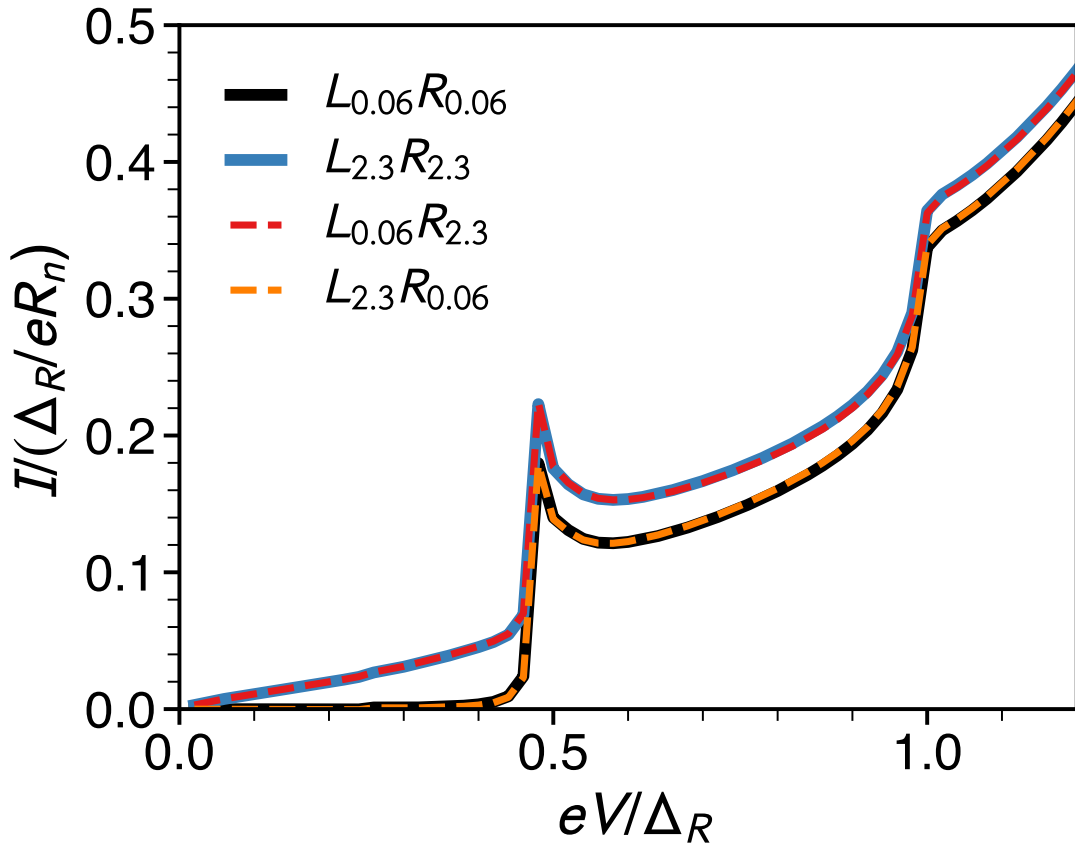


FIG. S.2. Calculated $I - V$ characteristics for different electrode temperatures with transparency $D = 0.25$, $\Delta_R = 1$ meV, and $\Delta_L = 0.5$ meV. The black line has $T_L = T_R = 0.06$ K. The blue line has $T_L = T_R = 2.3$ K. The dashed orange line lies on the black line but have $T_L = 2.3$ K and $T_R = 0.06$ K. The dashed red line has $T_L = 0.06$ K and $T_R = 2.3$ K, and lies on top of the blue line.

Appendix E: voltage-biased and current-biased characteristic

In the main paper, Fig. 7 shows current-biased $V(I)$ characteristics to show the detailed switching and retrapping currents. Figure S.3 shows $I(V)$ and $V(I)$ characteristics taken with a voltage and current bias for junction resistance (a)(b) $R_n = 57 \text{ k}\Omega$, (c)(d) $7.9 \text{ k}\Omega$ and (e)(f) $1.08 \text{ k}\Omega$. The brown curves and the orange curves represents the forward (from negative to positive voltage) and reverse sweep (from positive to negative voltage) from the voltage-biased mode, respectively. The blue and the black data represent the forward (from negative to positive current) and reverse sweep (from positive to negative current) from the current-biased mode. We see both the voltage-biased and the current-biased curves agree with each other well except the slight current drift due to noise when the feedback is turned off to acquire the curves. Additionally, there might also be a slow vertical drift when the feedback is off so the start point of the forward sweep and the end point of the reverse sweep are offset.

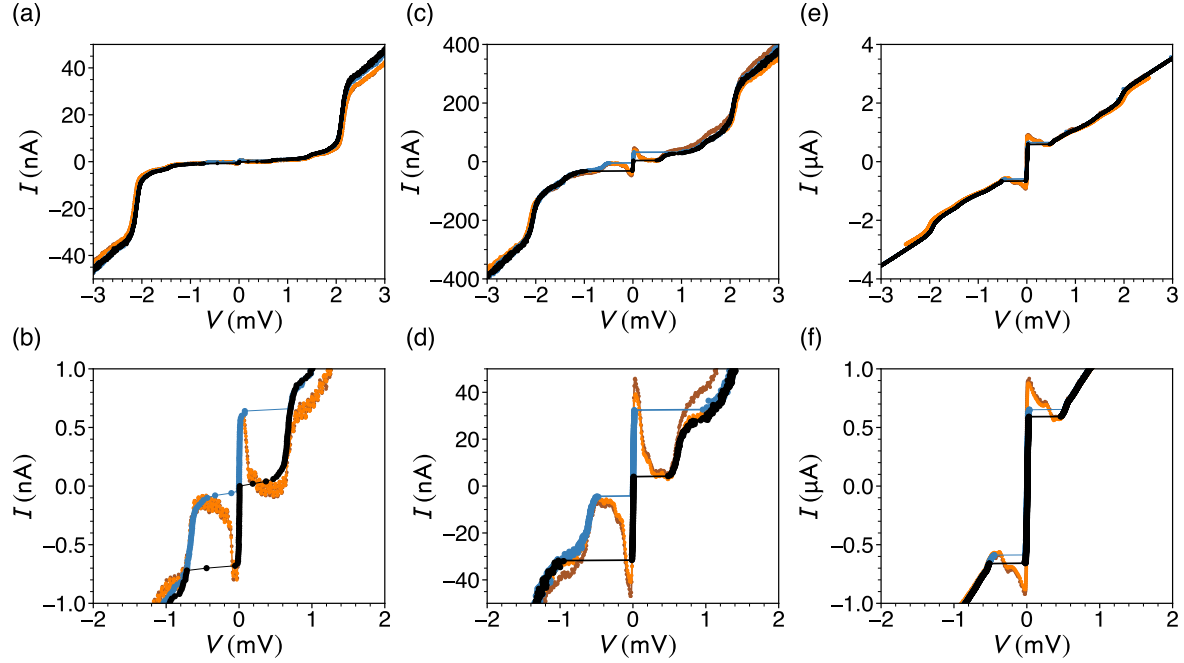


FIG. S.3. Current-voltage characteristics for junction tunneling resistance of (a)(b) $R_n = 57$ k Ω , (c)(d) 7.9 k Ω , and (e)(f) 1.08 k Ω measured with the voltage-biased mode and the current-biased mode. In each, the brown and orange lines show forward and reverse sweeps taken from the voltage-biased mode, and the blue and black points show forward and reverse sweeps taken from the current-biased mode.

Appendix F: dI/dV characteristic from the voltage-biased mode

The location of the peaks in the dI/dV curves from voltage-biased measurements $I(V)$ are sensitive to the superconducting gaps and transparencies. Here we show the dI/dV curves taken in the voltage biased mode. The lock-in frequency is 0.92 kHz with a drive amplitude $10 \mu\text{V}$. Figure S.4 shows the dI/dV characteristic for junction resistance (a) $R_n = 57 \text{ k}\Omega$, (b) $7.9 \text{ k}\Omega$ and (c) $1.08 \text{ k}\Omega$. The brown curves and the orange curves represent the forward sweep and the reverse sweep. The black dashed lines indicated indicate $V = \pm 2.13, \pm 1.5$, and $\pm 0.68 \text{ mV}$ and are at the same positions in the three plots as a guide to the eye. We can see that the peaks around the sample gaps Δ_s remain roughly the same even when the junction resistance is smaller. However the peaks around the tip gap Δ_t , and sum of the gaps $\Delta_t + \Delta_s$ decrease when the junction resistance becomes smaller.

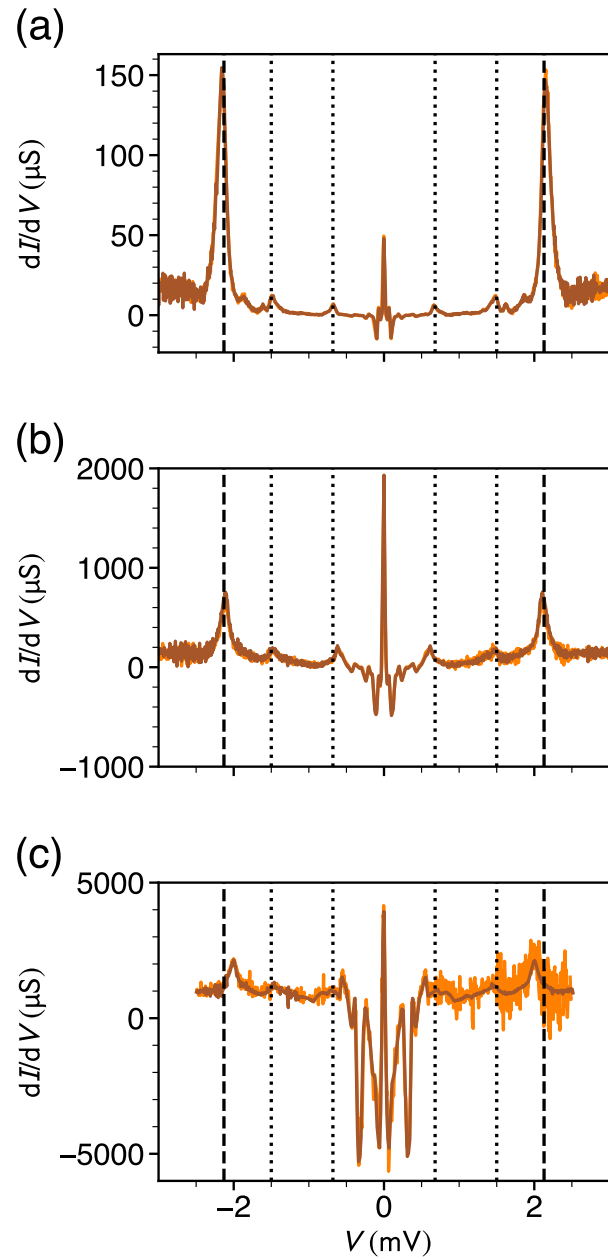


FIG. S.4. dI/dV characteristics for junction tunneling resistance of (a) $R_n = 57$ $k\Omega$, (b) 7.9 $k\Omega$, and (c) 1.08 $k\Omega$. The brown and orange curves show forward and reverse sweeps. The black dashed lines indicate $V = \pm 2.13, \pm 1.5$, and ± 0.68 mV.

Appendix G: Multi-channel fits

In this section, we motivate our decision to model the data with a non-integral number of effective conduction channels of a single transparency. In each panel of Fig. S.5, the $V(I)$ curve taken with a reverse sweep for $R_n = 35 \text{ k}\Omega$ is shown. Also plotted is the multi-channel MAR current $I(V) = \sum_{i=1}^N I_0(D_i, \Delta_s, \Delta_t, T, V)$ calculated for different values of N and D_i .

Figure S.5 (a) and (b) show results for $N = 1$. The measured values at large V are reproduced with $D = 0.335$, while much of the subgap structure is captured with $D = 0.230$. From this, it is clear that there must be multiple conduction channels, with $\sum D_i \approx 0.35$ and each $D_i < 0.230$.

In Fig. S.5 (c) and (d), curves for $N = 2$ show good agreement over the full voltage range, with a slight overestimate near the voltage corresponding to the tip gap. There is only a small difference at low voltage between identical channels and two channels with a spread in D . The low-voltage features can be better reproduced by adding a third channel with significantly lower transparency, as shown in Fig. S.5 (e) and (f).

Thus, we conclude that the current for this junction is predominantly carried by two channels, with identical channels producing good agreement. To characterize the transport at this R_n , we assume an effective channel number $N = 2.1$ with $D = 0.176$, as shown in Fig. S.5 (g) and (h).

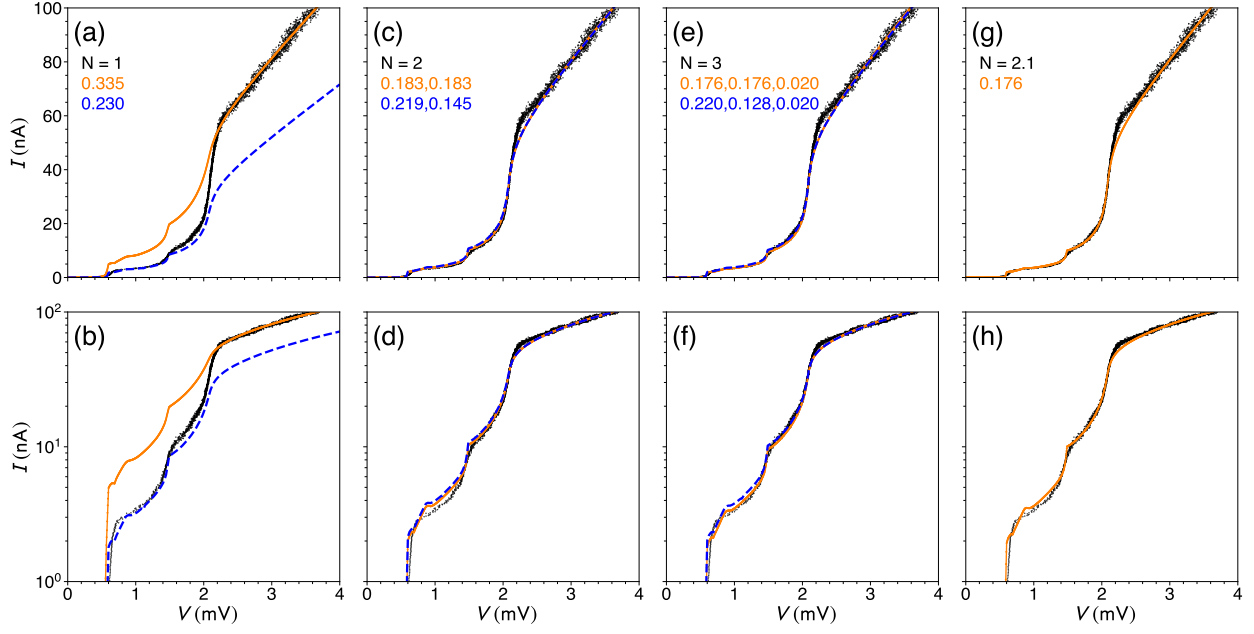


FIG. S.5. Comparison of multi-channel MAR $I - V$ characteristics (lines) with measured values of $V(I)$ (symbols) at $R_n = 35$ k Ω . The calculations correspond to (a) and (b) one, (c) and (d) two, (e) and (f) three channels, with the transparencies of the individual channels listed at the top of each column. (g) and (h) Good agreement to the data is found for a non-integral number of identical channels.

Appendix H: Conductance vs retraction-distance curves for various junction resistances

As we discussed in the main text, for $R_n < 5 \text{ k}\Omega$ the tip and the sample were probably in contact. To better understand this contact regime, we measured how the tunneling current at a fixed voltage bias varied with the distance of the tip from the surface. For these measurements, we set the junction resistance R_n (i.e. setting the value for I at a bias voltage of $V_b = 3.5 \text{ mV}$), measured the current setpoint I , and then found $R_n = V_b/I$. In the conventional tunneling limit, $I \propto e^{-\alpha z}$, where z is the distance between the tip and the sample. Thus, setting a smaller junction resistance R_n requires higher tunneling current, which results in smaller tip-sample separation. We then turned off the feedback and recorded the current I while retracting the tip. Figure S.6 shows the conductance $G = I/V_b$, normalized by the conductance quantum *vs* the retraction distance Δz . The measurement was repeated for six initial values of R_n , as labeled, although the curves were not acquired in the same order as the R_n values.

Examining Fig. S.6, for $5 \text{ k}\Omega < R_n < 12.9 \text{ k}\Omega$, the smallest steps are about $0.2 G_0$, signaling the tip is very close to the sample. Two orange curves starting at $R_n = 9.1 \text{ k}\Omega$, one curve shows a fairly smooth exponential-like dependence while the other shows similar behavior but with some small sudden jumps in conductance. It is possible that material was picked up or a slight deformation of the tip or sample occurred during the data acquisition of the first curve. Similar behaviors are also shown in $R_n = 7.0 \text{ k}\Omega$, and $5.7 \text{ k}\Omega$. In contrast, the curves with $R_n > 12.9 \text{ k}\Omega$ do not show conductance jumps. The red curves, which have an initial resistance of $3.2 \text{ k}\Omega$, show many large random jumps in conductance as the tip is withdrawn. Their behavior is probably due to different parts of the tip breaking contact with the sample at random times as the distance between the tip and sample increases. Therefore we can safely conclude that for $R_n < 5 \text{ k}\Omega$, the tip is making solid physical contact with the sample, causing deformation of the tip or sample, or the transfer of material between the tip and sample while retracting the tip from the sample. This result is comparable to behavior seen previously in break junctions, where the typical variations in conductance are of the order of G_0 [2, 10, 12, 38, 39].

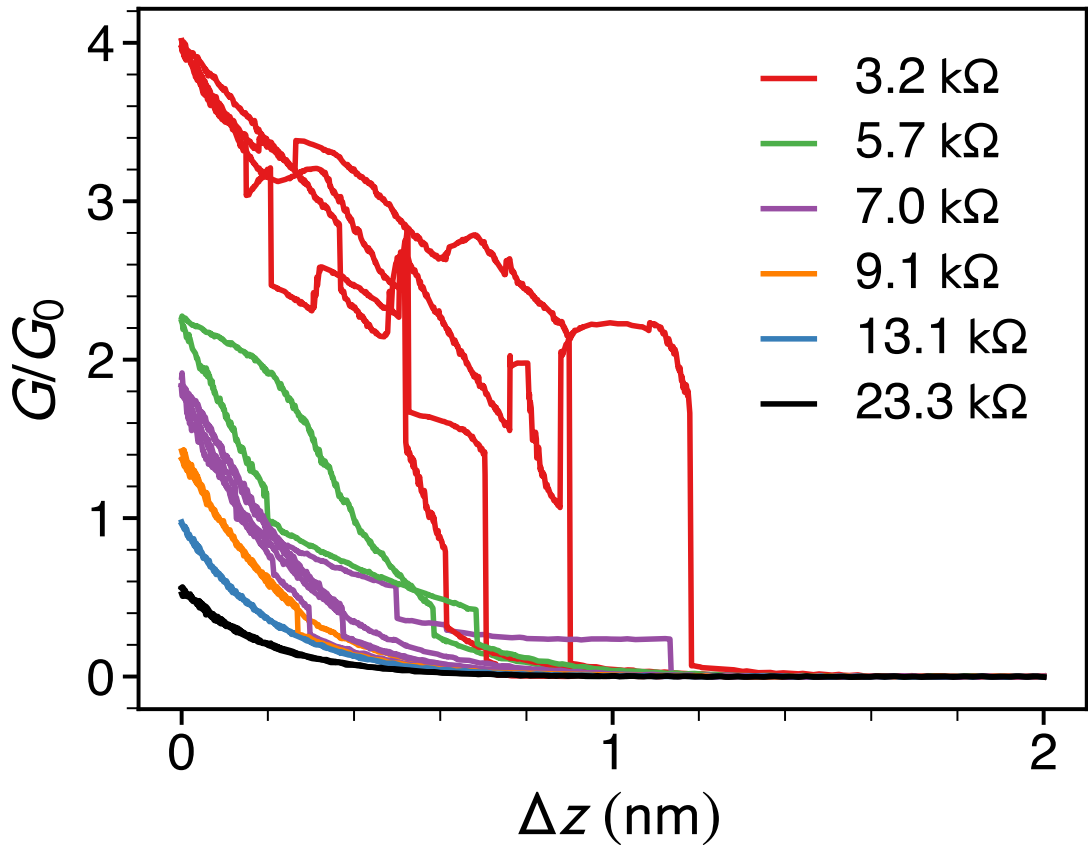


FIG. S.6. Normalized conductance G/G_0 vs Δz where $G_0 = e^2/(\pi\hbar)$ is the conductance quantum and Δz is the distance from the original tip position for different initial values of the tunnel resistance R_n . All measurements were made at $V_b = 3.5$ mV and $T = 1.5$ K. For $G \geq G_0$, the curves have occasional sudden jumps, suggesting the tip is forming a point contact with the surface. For $G > 3 G_0$, the tip probably makes solid contact with the sample and the large variation in conductance may be due to different parts of the tip leaving the surface at slightly different separations.

TABLE S1. symbol for different parameters

Switching current	I_s
Retrapping current	I_r
Critical current	I_c
Quasiparticle current	I_{qp}
Josephson energy	E_J
Coulomb charging energy	E_c
Plasma energy	$\hbar w_p$
Stewart-McCumber parameter	β_c